

# Algorithm-Oriented Qubit Mapping for Variational Quantum Algorithms

Yanjun Ji,<sup>1,\*</sup> Xi Chen,<sup>2,†</sup> Ilia Polian,<sup>1,‡</sup> and Yue Ban<sup>3,4,§</sup>

<sup>1</sup>*Institute of Computer Architecture and Computer Engineering,*

*University of Stuttgart, Pfaffenwaldring 47, 70569 Stuttgart, Germany*

<sup>2</sup>*Instituto de Ciencia de Materiales de Madrid (CSIC), Cantoblanco, E-28049 Madrid, Spain*

<sup>3</sup>*Departamento de Física, Universidad Carlos III de Madrid,*

*Avda. de la Universidad 30, 28911 Leganés, Spain*

<sup>4</sup>*TECNALIA, Basque Research and Technology Alliance (BRTA), 48160 Derio, Spain*

(Dated: July 30, 2024)

Quantum algorithms implemented on near-term devices require qubit mapping due to noise and limited qubit connectivity. In this paper we propose a strategy called algorithm-oriented qubit mapping (AOQMAP) that aims to bridge the gap between exact and scalable mapping methods by utilizing the inherent structure of algorithms. While exact methods provide optimal solutions, they become intractable for large circuits. Scalable methods, like SWAP networks, offer fast solutions but lack optimality. AOQMAP bridges this gap by leveraging algorithmic features and their association with specific device substructures to achieve optimal and scalable solutions. The proposed strategy follows a two stage approach. First, it maps circuits to subtopologies to meet connectivity constraints. Second, it identifies the optimal qubits for execution using a cost function. Notably, AOQMAP provides both scalable and optimal solutions for variational quantum algorithms with fully connected two qubit interactions on common subtopologies including linear, T-, and H-shaped, minimizing circuit depth. Benchmarking experiments conducted on IBM quantum devices demonstrate significant reductions in gate count and circuit depth compared to Qiskit, Tket, and SWAP network. Specifically, AOQMAP achieves up to an 82% reduction in circuit depth and an average 138% increase in success probability. This scalable and algorithm-specific approach holds the potential to optimize a wider range of quantum algorithms.

## I. INTRODUCTION

Recent strides in variational quantum algorithms (VQAs) [1, 2] have demonstrated considerable potential in solving complex problems, such as combinatorial optimization [3] and quantum simulation of materials [4], surpassing the efficiency of classical algorithms. However, existing constraints of quantum processing units (QPUs) pose a significant obstacle to realizing the full capabilities of VQAs. A major challenge is the presence of noise, limited number of qubits, and restricted connectivity between qubits. These constraints impede the scalability and applicability of VQAs in tackling larger and more intricate problems. Efforts to overcome these challenges are critical for unlocking the complete potential of VQAs in practical applications. Specifically, the execution of quantum algorithms requires compilation before being deployed on a quantum device, which involves addressing connectivity constraints by introducing SWAP gates and decomposing algorithms into native hardware basis gates. Moreover, optimizing circuits to minimize the influence of noise is crucial to ensure accurate performance of algorithms [5].

A crucial step in compilation is mapping logical qubits to physical qubits available on quantum devices, a com-

plex problem commonly referred to as qubit mapping [6–10]. The main objective of qubit mapping is to minimize the number of inserted SWAP gates or circuit depth and to maximize circuit fidelity. This problem is identified as NP-hard [11], underscoring the necessity for efficient and effective methods to tackle it. Qubit mapping can be expressed as a mathematical optimization problem and solved using constraint satisfaction techniques. These approaches are called exact methods and have been investigated in various studies [12–16]. While exact methods provide high quality and stable solutions, their compilation time increases exponentially with problem size. In contrast, heuristic approaches [9, 14, 15, 17–19] prioritize efficiency by providing fast solutions without guaranteeing optimality. Another approach involves constructing swap layers [20–24] aimed at providing scalable solutions. However, similar to heuristic methods, optimality is not guaranteed.

This paper proposes an efficient, two-stage approach to qubit mapping, prioritizing both optimality and scalability. In the first stage, quantum algorithm is mapped to the target QPU's subtopologies to address connectivity constraints. Here, we provide optimal and scalable solutions with minimal circuit depth for VQAs with all-to-all connected two qubit interactions on common subtopologies including linear, T-, and H-shaped. For VQAs with partially connected two qubit interactions, solutions can be obtained by optimizing the initial qubit order to minimize CX gate count. These solutions are applicable to various noisy intermediate scale quantum (NISQ) devices, such as Google's Sycamore, IBM's QPUs, and Rigetti's processors. After addressing connectivity con-

\* yanjun.ji@informatik.uni-stuttgart.de

† xi.chen@csic.es

‡ ilia.polian@informatik.uni-stuttgart.de

§ ybanxc@gmail.com

straints, the second stage focuses on selecting optimal qubits for execution. The subtopology-adapted circuit is mapped onto the QPU taking into account its current noise information. All compatible subtopologies are identified, and the one minimizing circuit error is chosen.

Unlike conventional methods that usually map predefined circuits, our approach begins directly from the algorithm's Hamiltonian, allowing for optimization during the conversion process from Hamiltonian to circuit representation. This codesign strategy generates mappings tailored to the algorithm's structure and hardware constraints. This methodology promises not only optimality but also enhanced adaptability and scalability in tackling the qubit mapping challenge. Benchmarks on six IBM QPUs with 7, 27, and 127 qubits demonstrate significant performance gains. In particular, we achieve an average reduction of 31% (up to 82%) in circuit depth and an average increase of 138% in success probability compared to Qiskit [25], Tket [26], and SWAP network [20].

The paper is structured as follows. Section II provides background on NISQ devices and the qubit mapping problem. Section III details our proposed approach, including the analysis of subtopology solutions and mapping strategies for adapted circuits. Section IV demonstrates practical applications of our method to VQAs, in particular the quantum approximate optimization algorithm (QAOA) and variational quantum eigensolver (VQE). Section V presents benchmarking results comparing our technique to existing methods on QPUs. Finally, Sec. VI concludes.

## II. BACKGROUND

### A. Near-term quantum devices

Prominent near-term quantum platforms exhibit distinctive characteristics. Superconducting qubits, for instance, demonstrate increased connectivity that extends beyond nearest neighboring qubits [27–29], while trapped ions showcase relatively long coherence times [30], and photons exhibit low noise [31]. In the era of NISQ computing [32], the development of practical algorithms encounters substantial constraints due to the inherent limitations of quantum hardware. For instance, the 7-, 27-, and 127-qubit IBM QPUs illustrated in Fig. 1, exhibit restricted connectivity. Specifically, each qubit can only directly interact with up to three neighboring qubits. Additionally, the noise in quantum systems varies over time, leading to temporal fluctuations in errors. These hardware limitations pose challenges for implementing quantum algorithms that rely on long-range qubit interactions or high precision. Current endeavors concentrate on enhancing the control of qubits by improving coherence times, elevating gate fidelities, and expanding qubit connectivity. Moreover, compiling quantum algorithms to reduce circuit depth and mitigate errors is essential to fully realizing the potential of these devices.

To address the limitations of NISQ devices, researchers have developed VQAs [1], which are hybrid algorithms combining classical optimization techniques with quantum resources. However, implementing VQAs on NISQ devices presents challenges. One significant hurdle is selecting an appropriate classical optimization algorithm, which can profoundly impact the success of VQAs. Moreover, mapping algorithms onto physical qubits of quantum devices, especially for larger circuits, is difficult. Strategies to tackle these challenges have been developed, such as employing machine learning techniques to optimize parameters [33], developing new ansatz to capitalize on qubit connectivity [34], and implementing efficient compilation processes [35–40]. In this study, our focus is on efficient qubit mapping, which is a crucial step in implementing VQAs. We examine the challenges and opportunities associated with qubit mapping and propose an approach to improve scalability and optimality. We assess the effectiveness of our approach and demonstrate its application on real quantum hardware.

### B. Qubit mapping problem

The primary objective of qubit mapping is to minimize errors inherent in the implementation of algorithms on QPUs. This task is critical in mitigating errors arising from the noisy nature of qubits, particularly in the context of high error rates associated with two-qubit gates such as CNOT or CX that can significantly impact the overall performance of algorithms. Optimizing the qubit mapping process requires a careful balance between two crucial factors. First, the insertion of SWAP gates introduces errors when connecting two qubits that are not directly linked, as the implementation of a SWAP gate necessitates three CX gates. Second, the quality of qubits and qubit pairs can vary, necessitating the identification of the most suitable qubits for circuit execution. While searching for solutions of qubit mapping on a specific subtopology can markedly reduce computational complexity compared to exploring solutions across the entire topology, particularly for larger topologies with hundreds of qubits, it's crucial to strike the right balance between the number of SWAP gates inserted on specific topologies and the quality of qubits on those topologies.

## III. METHODOLOGY AND PRELIMINARIES

This section details our methodology. Figure 2 presents algorithm oriented qubit mapping (AOQMAP) flow. The process begins with decomposition of input VQA into a two qubit Hamiltonian. Subsequently, this Hamiltonian is routed onto subtopologies by introducing SWAP gates, ensuring compliance with hardware connectivity constraints. Each of these routed circuits is then decomposed into native basis gates of target QPU and optimized to minimize errors. For verification, a refer-

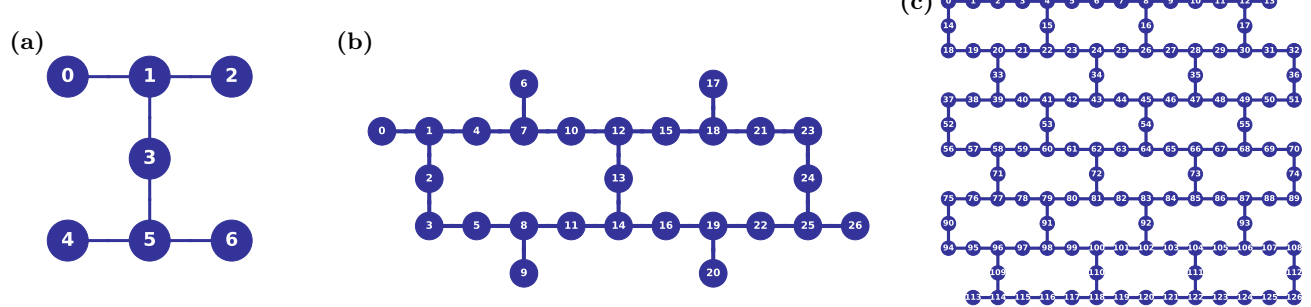


FIG. 1. Topologies of IBM QPUs with (a) 7, (b) 27, and (c) 127 qubits. Circles denote individual qubits. Lines connecting the circles represent available two-qubit gates between corresponding qubit pairs.

TABLE I. Number of layouts within a 27-qubit QPU that enable the execution of circuits satisfying the connectivity constraints of subtopologies shown in Figs. 3(a-o).

Topology	3	4	5	6	7
Linear	74 (a)	80 (b)	100 (d)	104 (f)	132 (j)
T-shaped		48 (c)	36 (e)	64 (g)	48 (k)
H-shaped				56 (l)	
T-variant			24 (h-i)	44 (m-n), 12 (o)	

ence circuit is constructed directly from the two-qubit Hamiltonian, matching parameters and gate sequences of routed circuit. The Hellinger distance between output distributions of reference and routed circuits is employed to ensure correctness. Finally, a cost function is utilized to select the optimal set of qubits for execution. This comprehensive flow guarantees effective adaptation, verification, and optimization of quantum circuits within constraints imposed by target hardware topology.

We identify three common types of subtopologies within the qubit connectivity graph of target device. This is performed by first identifying all possible subtopologies within a 27-qubit QPU shown in Fig. 1(b) and then calculating all layouts within the QPU that allow execution of circuits on such subtopologies using mapomatic [41]. Figure 3 presents identified subtopologies for qubit counts ranging from 3 to 7. The corresponding counts of layouts for each subtopology in Fig. 3 are summarized in Table I. Our analysis reveals that linear, T-, and H-shaped subtopologies are the most common for the problem sizes studied. Therefore, we focus on these three types and provide optimal and scalable solutions for VQAs with fully connected two qubit interactions on such subtopologies.

### A. Subtopology-aware circuit adaptation

This section introduces the methodology for subtopology aware circuit adaptation on NISQ devices. We focus on linear, T-, and H-shaped configurations, and develop

strategies for adapting VQAs to each subtopology.

In this study, we focus on the QAOA applied to dense portfolio optimization problems, where each qubit necessitates interaction with all other qubits. As detailed in Ref. [42], the problem Hamiltonian for  $n$  asset portfolio optimization is expressed as

$$H_c = \sum_{i=1}^{n-1} \sum_{j=i+1}^n c_{ij} Z_i Z_j + \sum_{i=1}^n c_i Z_i + c_0. \quad (1)$$

Here,  $Z_i Z_j$  represents  $ZZ$  interaction between qubits  $i$  and  $j$ , defined by  $ZZ(\theta) = e^{-i\frac{\theta}{2}Z \otimes Z}$  with rotation angle  $\theta$ .  $Z_i$  denotes Pauli  $Z$  operator acting on qubit  $i$ . The coefficients  $c_{ij}$ ,  $c_i$ , and  $c_0$  are real numbers determined by parameters in the portfolio optimization problem. We consider the mixing operator in QAOA with the form

$$H_m = \sum_{i=1}^n X_i, \quad (2)$$

where  $X_i$  is Pauli  $X$  operator acting on qubit  $i$ . The QAOA commences by selecting an initial state, denoted by  $|\psi_0\rangle$ , which is the eigenstate of mixer Hamiltonian  $H_m$ . Subsequently, problem and mixer Hamiltonians are applied alternately to  $|\psi_0\rangle$  in a parameterized quantum circuit of depth  $p$ . This yields a quantum state

$$|\psi_{\gamma, \beta}\rangle = \sum_{k=1}^p e^{-i\beta_k H_m} e^{-i\gamma_k H_c} |\psi_0\rangle, \quad (3)$$

where  $\beta, \gamma$  are  $p$ -dimensional vectors of rotation angles that control the evaluation of  $H_c$  and  $H_m$  in each layer  $k$ . The  $2p$  parameters  $(\gamma, \beta)$  can be optimized using a classical solver to minimize the expectation value  $\langle \psi_{\gamma, \beta} | H_c | \psi_{\gamma, \beta} \rangle$ . This tuning process adjusts  $|\psi_{\gamma, \beta}\rangle$  to approximate the ground state of  $H_c$ , offering a well-approximated solution to the optimization problem encoded in  $H_c$ .

To achieve optimal qubit mapping solutions, a comprehensive analysis of problem and mixer Hamiltonians described in Eqs. (1) and (2) is essential. Notable observations guide our approach: (i) The two-qubit gates in

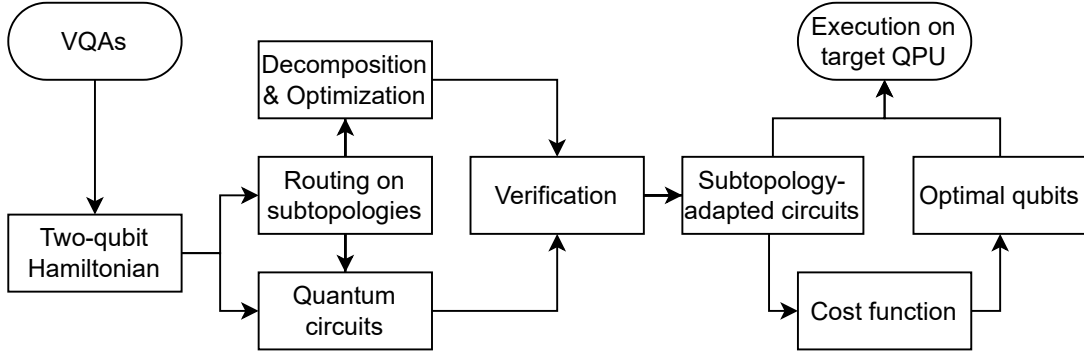


FIG. 2. Algorithm-oriented qubit mapping (AOQMAP) flow is outlined for mapping VQAs onto a target QPU. The AOQMAP approach differs from traditional qubit mapping methods in that it starts from a two-qubit Hamiltonian, rather than a predefined circuit. The process of AOQMAP involves two main steps: (1) adapting VQA to subtopologies of target QPU; and (2) selecting the optimal mapping scheme to implement subtopology-adapted circuits. The adaptation process ensures algorithm excitability, while the mapping process guarantees the use of high-quality qubits for execution. By first adapting circuits and then choosing an optimal mapping scheme, AOQMAP minimizes errors and optimizes algorithm performance.

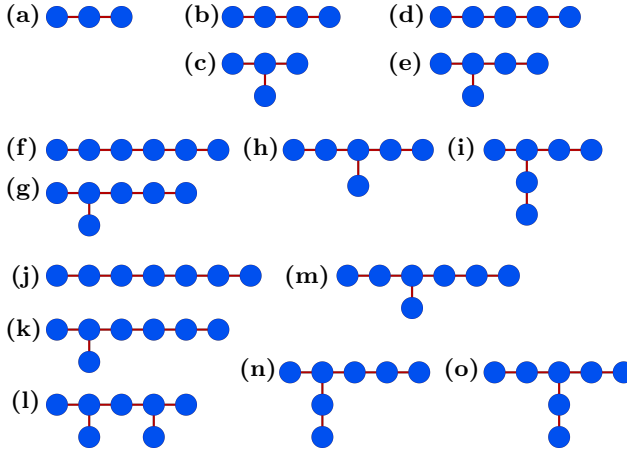


FIG. 3. All possible subtopologies within the heavy-hex topology for varying numbers of qubits, ranging from 3 to 7. The most common subtopology on a 27-qubit topology (Fig. 1(b)) is linear, followed by T-shaped and then H-shaped.

Eq. (1) exclusively involve  $ZZ$  interactions. Their summation form implies that the order of application does not affect the outcome, allowing flexibility in mapping  $H_c$ ; (ii) The single rotation gates  $R_Z$  and  $R_X$  in  $H_c$  and  $H_m$  can be independently applied to each qubit without affecting others. Hence, qubit mapping is unnecessary for these gates; (iii) For high depths, as depicted in Eq. (3), a fixed gate arrangement for two-qubit gates is required at each depth to maintain an equivalent  $H_c$ . However, since all  $ZZ$  gates commute with each other, they can be assigned in each depth with an arbitrary gate arrangement. This implies that the  $ZZ$  gate arrangement needed for implementing QAOA at each depth can be arbitrary, providing additional flexibility in qubit mapping. By leveraging these observations, we can formulate a tailored mapping method for quantum algorithms to opti-

mize their performance, minimizing the number of CX gates, reducing circuit depth, and thereby maximizing the algorithm's overall performance.

In the upcoming sections, we explore qubit mapping solutions on three subtopologies, emphasizing QAOA with all-to-all connected two-qubit gate interactions. Although our analysis focuses on this specific instance of VQAs, the implications extend to algorithms with analogous features. Specifically, we underscore the relevance of our findings to Hamiltonian with partially connected interactions, VQE, and other NISQ devices in Sec. IV.

### 1. Linear subtopology

In quantum computing, linear subtopology arranges qubits sequentially in a one-dimensional configuration, forming a linear chain or arrangement. To determine optimal mapping on this subtopology, we initially employ an exact method aimed at minimizing the circuit depth [16]. However, instead of mapping the entire algorithm, we focus solely on mapping the  $ZZ$  gates in Eq. (1), treating them as single entities and avoiding the decomposition into two CX gates to streamline the mapping process. Additionally, we narrow our attention to the first QAOA depth, significantly reducing the effort required to identify a solution.

The routing solution for  $ZZ$  gates in a five-qubit QAOA on linear topology is illustrated in Fig. 4(a). Assuming an arbitrary initial qubit order  $[a, b, c, d, e]$ , after each swap layer, qubit orders evolve as follows:  $[a, c, b, e, d]$ ,  $[c, a, e, b, d]$ , and  $[c, e, a, d, b]$ . Since each qubit needs to interact with all other qubits,  $ZZ$  gate acts on following qubit pairs: for qubit  $a$ ,  $(a, b)$ ,  $(a, c)$ ,  $(a, d)$ , and  $(a, e)$ ; for qubit  $b$ ,  $(b, c)$ ,  $(b, d)$ , and  $(b, e)$ ; for qubit  $c$ ,  $(c, d)$ , and  $(c, e)$ ; and for qubit  $d$ ,  $(d, e)$ . Our analysis reveals that all ten  $ZZ$  gates required in a five-qubit QAOA can be

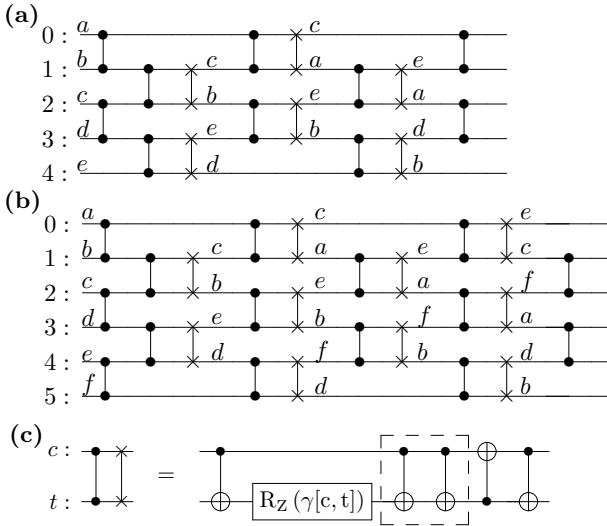


FIG. 4. Routing solutions of ZZ gates in QAOA at depth  $p = 1$  with (a) five and (b) six qubits. (c) ZZ gate on qubit pair  $(c, t)$  with rotation angle  $\gamma[c, t]$ , followed by a SWAP gate, with the box showing CX gate cancellation between ZZ and SWAP gates.

executed on a linear subtopology, regardless of the initial qubit order. This observation is highly beneficial for achieving scalability, as it facilitates straightforward extension to high QAOA depths by repeating these swap layers. Similarly, as depicted in Fig. 4(b), the fifteen ZZ gates required for six-qubit QAOA can be implemented using four swap layers. We observe that in an  $n$ -qubit QAOA, ZZ gates are organized into  $n$  layers to minimize circuit depth. The swap layers, excluding the first and last layers, are positioned after each ZZ layer. As shown in Fig. 4(c), due to the cancellation of CX gates between ZZ and SWAP gates, each SWAP gate following a ZZ gate introduces only one additional CX gate. The optimal routing solutions of ZZ gates in QAOA on linear subtopology exhibit a structure similar to the SWAP network presented in Ref. [20], with the absence of the first and last swap layers. This similarity enables the extension of solutions to an arbitrary number of qubits. The dispensability of the first and last swap layers stems from the flexibility to adjust initial qubit order and measurement order to eliminate SWAP gates in the first and last ZZ layers, leveraging commutativity of ZZ and SWAP gates. Once two-qubit gates are mapped, we can construct the entire QAOA circuit.

Algorithm 1 presents pseudocode for mapping QAOA on linear subtopology. The reconstruction process starts with an initialized qubit order  $O = \{0, 1, \dots, i, \dots, j, n - 1\}$  for  $n$  qubits. We first prepare an initial state  $|\psi_0\rangle$  by applying a Hadamard gate to each qubit. Then, we apply ZZ or ZZ-SWAP gate layer continuously according to the solutions presented in Fig. 4. The order of qubits  $i$  and  $j$  is exchanged only when a SWAP gate is applied to qubit pair  $(i, j)$ . To improve algorithm efficiency, it is

---

**Algorithm 1:** AOQMAP for QAOA on linear subtopology

---

**Input:** Number of qubits  $n$ , QAOA depth  $p$ , Parameters  $\gamma[c, t]$ ,  $\alpha[i]$ , and  $\beta[j]$  of gates ZZ on qubit pair  $(c, t)$ , Rz on qubit  $i$ , and Rx on qubit  $j$ , respectively, where  $c, t, i, j \in \{0, \dots, n - 1\}$  and  $c < t$

**Output:** Circuit satisfying connectivity constraints

```

1 Function ApplyZZGate( $O, i, j$ )
2   | Apply ZZ( $\gamma[O[i], O[j]]$ ) on  $(i, j)$ 
3 end
4 Function ApplyZZSWAPGate( $O, i, j$ )
5   | Apply ZZ( $\gamma[O[i], O[j]]$ ) on  $(i, j)$ 
6   | Apply SWAP on  $(i, j)$ 
7   |  $O[i] \leftrightarrow O[j]$  // Exchange qubit order
8 end
9  $O \leftarrow \{0, 1, \dots, n - 1\}$  // Initialize the qubit order
10 Prepare the initial state  $|0\rangle^{\otimes n}$ 
11 Apply  $H^{\otimes n}$ 
12 while  $p > 0$  do
13   |  $s \leftarrow 0$ 
14   | while  $s < n$  do
15     |   | for  $q := 0$  to  $n - 1$  step 2 do
16       |   |   | if  $s == 0$  or  $s == n - 1$  then
17       |   |   |   | ApplyZZGate( $O, q, q + 1$ )
18       |   |   | else
19       |   |   |   | ApplyZZSWAPGate( $O, q, q + 1$ )
20       |   | end
21   | end
22   |  $s \leftarrow s + 1$ 
23   | if  $s < n$  then
24     |   | for  $q := 1$  to  $n - 1$  step 2 do
25       |   |   | if  $s == 0$  or  $s == n - 1$  then
26       |   |   |   | ApplyZZGate( $O, q, q + 1$ )
27       |   |   | else
28       |   |   |   | ApplyZZSWAPGate( $O, q, q + 1$ )
29       |   | end
30   | end
31 end
32 |  $s \leftarrow s + 1$ 
33 end
34 for  $k := 0$  to  $n$  do
35   | Apply Rz( $\alpha[O[k]]$ ) on  $k$ 
36   | Apply Rx( $\beta[O[k]]$ ) on  $k$ 
37 end
38 |  $p \leftarrow p - 1$ 
39 end
40 Measure the qubits  $([0, \dots, n - 1] \rightarrow [O[0], \dots, O[n - 1]])$ 

```

---

crucial to optimize ZZ and ZZ-SWAP gates using strategies such as gate cancellation or pulse level optimization techniques [43]. Finally, Rz gates in problem Hamiltonian and Rx gates in mixer Hamiltonian are implemented on qubits with appropriate parameters. Figure 5 shows the resulting circuit of a five-qubit QAOA at depth  $p = 1$ . All ZZ, Rz, and Rx gates are executed according to the current qubit order, followed by measurement of qubits.

As demonstrated, an arbitrary qubit order can implement all required ZZ gates in QAOA with  $n$  qubits using

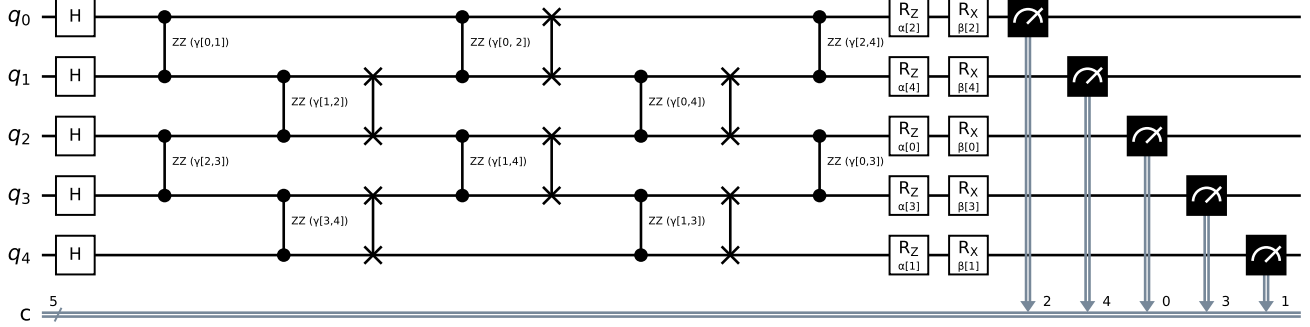


FIG. 5. Resulting circuit of five-qubit QAOA for portfolio optimization on a linear subtopology using AOQMAP approach. This circuit is further decomposed and optimized for the target QPU. The optimal mapping scheme is then selected for execution based on the QPU’s noise information.

$n - 2$  swap layers. A solution of depth  $p$  can be obtained by repeating  $p$  times swap layers in depth  $p = 1$  circuit. Inserting these swap layers consecutively, the initial order returns after  $2n$  swap layers. Since each QAOA depth introduces  $n - 2$  swap layers, circuit repeats every  $\text{lcm}(2n, n - 2)/(n - 2)$  depths, where  $\text{lcm}(2n, n - 2)$  is the least common multiple of  $2n$  and  $n - 2$ . For odd numbers of qubits, one repetition of swap layers in depth  $p = 1$  circuit demonstrates symmetry, and at depth two, the final qubit order returns directly to the initial qubit order. For even numbers of qubits, one repetition of such swap layers demonstrates alternating odd and even-numbered swap layers, resulting in circuits that repeat a subcircuit with the same gate arrangement every  $\text{lcm}(2n, n - 2)/(n - 2)$  layers. Since all ZZ gates commute with each other, these two constructions of high depth solutions are equivalent. However, we can utilize mirror symmetry of swap layers to construct high depth circuits for even numbers of qubits and obtain circuits repeating every two depths. Additionally, mirror symmetry can also be utilized to construct algorithms with partially connected two qubit gates, which we discuss in Sec. IV.

## 2. T-shaped subtopology

We now analyze solutions obtained by exact method [16] for two-qubit gates in QAOA with five and six qubits on T-shaped subtopology. A T-shaped subtopology features a central qubit at the apex of “T” shape, serving as the primary qubit. The arms of T-shaped topology consist of one or more qubits that are linearly connected to the central qubit. The qubits in arms typically do not have direct interactions with each other. We note that the minimum number of qubits on a T-shaped subtopology is four. Figure 6(a) shows the definition of T-shaped topology for  $n$  qubits with qubit 2 as the center qubit. Consider an arbitrary initial qubit order  $[a, b, c, d, e]$  for the solution of five-qubit,

---

### Algorithm 2: Swap layers on T-shaped subtopology

---

**Input:** Number of qubits  $n$ , Connectivity of T-shaped topology defined in Fig. 6(a)  
**Output:** List of swap layers  $S$

```

1 begin
2    $n_{\text{odd}} \leftarrow (n - 1) - 1 + (n - 1) \bmod 2;$ 
3    $n_{\text{even}} \leftarrow (n - 1) - (n - 1) \bmod 2;$ 
4    $S \leftarrow \text{empty List};$ 
5    $j \leftarrow 0;$ 
6   while  $j < n$  do
7      $S[j] \leftarrow S[j] \cup [(2, 3), (4, 5), \dots, (n_{\text{odd}} - 1, n_{\text{odd}})];$ 
8     if  $++j \geq n$  then break;
9      $S[j] \leftarrow S[j] \cup [(0, 2), (3, 4), \dots, (n_{\text{even}} - 1, n_{\text{even}})];$ 
10    if  $++j \geq n$  then break;
11     $S[j] \leftarrow S[j] \cup [(2, 3), (4, 5), \dots, (n_{\text{odd}} - 1, n_{\text{odd}})];$ 
12    if  $++j \geq n$  then break;
13     $S[j] \leftarrow S[j] \cup [(1, 2), (3, 4), \dots, (n_{\text{even}} - 1, n_{\text{even}})];$ 
14    if  $++j \geq n$  then break;
15  end
16 end

```

---

as shown in Fig. 6(b). Following each swap layer, the qubit order evolves sequentially:  $[a, b, d, c, e]$ ,  $[d, b, a, e, c]$ , and  $[d, b, e, a, c]$ . This sequence allows us to execute all required ten ZZ gates for five-qubit QAOA. Similarly, the four swap layers in six-qubit QAOA are capable of performing the necessary fifteen ZZ gates, as shown in Fig. 6(c).

Algorithm 2 outlines procedure for generating  $n$  swap layers for  $n$ -qubit QAOA on T-shaped subtopology. As depicted in Fig. 6(c), the initial swap layer starts at center qubit 2 and consists of SWAP gates on qubit pairs  $\{(2, 3), (4, 5), \dots, (n_{\text{odd}} - 1, n_{\text{odd}})\}$  with  $n_{\text{odd}} = (n - 1) - 1 + (n - 1) \bmod 2$ . This layer alternates with another layer that starts from two different qubits in short arms of a T-shaped structure, forming two distinct layers  $\{(0, 2), (3, 4), \dots, (n_{\text{even}} - 1, n_{\text{even}})\}$  and  $\{(1, 2), (3, 4), \dots, (n_{\text{even}} - 1, n_{\text{even}})\}$  with  $n_{\text{even}} = (n - 1) - (n - 1) \bmod 2$ . After constructing  $n$  swap layers, all re-

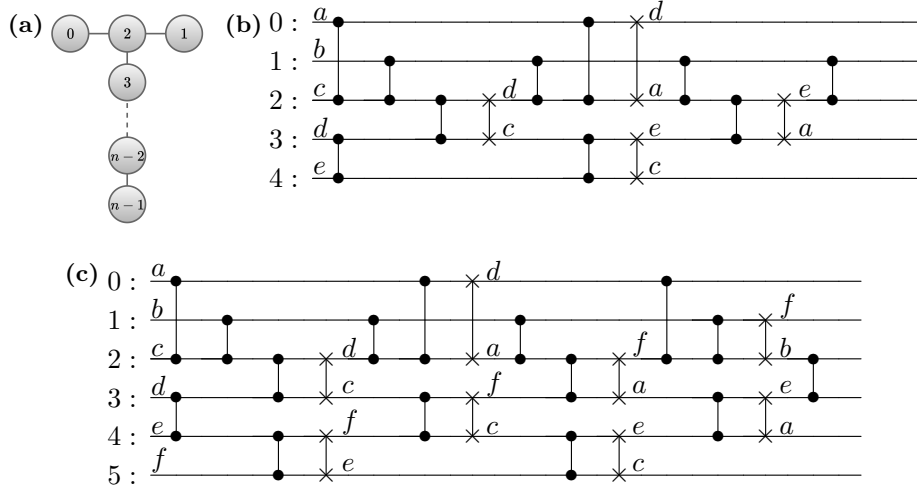


FIG. 6. Definition of T-shaped topology and corresponding routing solutions of ZZ gates in QAOA at depth  $p = 1$ . (a) T-shaped topology defined for  $n$  qubits with qubit 2 as the center qubit. The connectivity of this subtopology for  $n$  qubits is given by  $\{(0, 2), (1, 2), (2, 3), (3, 4), \dots, (n - 2, n - 1)\}$ . (b) Five-qubit routing solution. (c) Six-qubit routing solution.

quired ZZ gates can be implemented on connected qubit pairs. Algorithm 3 presents pseudocode for AOQMAP applied in  $n$ -qubit QAOA at depth  $p = 1$  on T-shaped subtopology. We begin the process by initializing a qubit order  $O = \{0, 1, \dots, i, \dots, j, n - 1\}$  for  $n$  qubits, with qubit 2 being center qubit. This initial qubit order enables executing one layer of ZZ gates. One possible option is gates on qubit pairs of the center qubit and two qubits in short arm, and gates on qubit pairs starting with the first qubit in long arm. For instance, the first ZZ layer in six-qubit QAOA consists of  $\{(0, 2), (1, 2), (3, 4)\}$ . The second layer starts with center qubits and proceeds to qubits on long arm to form ZZ gates on qubit pairs  $\{(2, 3), (4, 5)\}$ , followed by the first swap layer that introduces new qubit order and provides opportunity for additional gate implementation. We first execute rest ZZ gates that are not on qubit pairs of the second swap layer. Then, we implement remaining ZZ gates on qubit pairs of the second swap layer, followed by SWAP gates. This process ensures that ZZ gate is positioned immediately before SWAP gate on the corresponding qubit pair, thereby enabling CX gate cancellation. We maintain this iterative process until all ZZ gates are implemented.

Similar to linear subtopology, there are two solutions for higher depths: repeating swap layers in depth  $p = 1$  circuit and leveraging mirror symmetry of swap layers. Alternating swap layers and their mirrors causes gates in QAOA at depth  $p$  to invert gates at the previous depth. For commuting gates such as the ZZ gates used in QAOA, this reversal has no impact on algorithm performance. However, for noncommuting gates, this inversion may suppress Trotter errors [44, 45], making AOQMAP promising for optimizing other algorithms. Compared to solutions on linear topology that exhibit a fixed number

of swap layers, solutions on T-shaped topology require at least  $n - 2$  but no more than  $n$  swap layers for  $n$ -qubit QAOA. If ZZ gates remain after  $n - 2$  swap layers, SWAP gates in the penultimate and/or last layer become indispensable. It is worth noting that SWAP gates at the end of a circuit can be eliminated, as no remaining two-qubit gates require the introduction of new qubit orders.

The T-shaped subtopology affords enhanced qubit connectivity for the central qubit, reducing required SWAP gates but increasing circuit depth. This implies that T-shaped subtopology is advantageous when the algorithm's fidelity is a primary factor affecting performance. Conversely, linear subtopology is more effective for larger circuit sizes where schedule duration is paramount.

### 3. H-shaped subtopology

The H-shaped subtopology shares similarities with T-shaped, but has two central qubits at each end instead of one. The horizontal segments of “H” serve as a bridge connecting central qubits. To implement an H-shaped subtopology, a minimum of six qubits is required. We define the connectivity of an H-shaped subtopology with center qubits 2 and  $n - 3$  as  $\{(0, 2), (1, 2), (2, 3), \dots, (n - 4, n - 3), (n - 3, n - 2), (n - 3, n - 1)\}$  for  $n$  qubits.

Algorithm 4 presents pseudocode for generating  $n$  swap layers that enable the implementation of Hamiltonian with fully connected two-qubit gates on H-shaped topology. All  $n$  swap layers are necessary for this implementation. For odd numbers of qubits, the first and third swap layers differ in initial connections of  $(0, 2)$  and  $(1, 2)$ , which alternate. Similarly, the second and fourth layers differ in final connections of  $(n_{\text{even}} - 2, n_{\text{even}} - 1)$  and

---

**Algorithm 3:** AOQMAP for QAOA at depth  $p = 1$  on T-shaped subtopology

---

**Input:** Number of qubits  $n$ , Parameters  $\gamma[c, t]$ ,  $\alpha[i]$ , and  $\beta[j]$  of gates ZZ on qubit pair  $(c, t)$ ,  $R_Z$  on qubit  $i$ , and  $R_X$  on qubit  $j$ , respectively, where  $c, t, i, j \in \{0, \dots, n-1\}$  and  $c < t$

**Output:** Circuit satisfying connectivity constraints

```

1  $O \leftarrow \{0, 1, \dots, n-1\}$  // Initialize the qubit order
2  $L \leftarrow$  List of all ZZ gates
3  $E \leftarrow$  List of connected edges on T-shaped subtopology
4  $E_O \leftarrow [(O[r], O[s]) \text{ for } (r, s) \in E]$ 
5  $S \leftarrow$  List of  $n$  swap layers // Algorithm 2
6  $S_O \leftarrow [(O[r], O[s]) \text{ for } (r, s) \in S[k]]$ 
7 Function ApplyZZGate( $O, c, t$ )
8   | Apply ZZ( $\gamma[c, t]$ ) on  $(O.\text{index}(c), O.\text{index}(t))$ 
9 end
10 Function ApplySWAPGate( $O, i, j$ )
11   | Apply SWAP on  $(i, j)$ 
12   |  $O[i] \leftrightarrow O[j]$  // Exchange qubit order
13 end
14 Prepare the initial state  $|0\rangle^{\otimes n}$ 
15 Apply  $H^{\otimes n}$ 
16 for  $k := 0$  to  $n$  do
17   | if  $L$  is empty then continue
18   | foreach ZZ( $\gamma[c, t]$ ) in  $L$  do
19   |   | if  $(c, t) \in E_O$  and  $(c, t) \notin S_O$  then
20   |   |   | ApplyZZGate( $O, c, t$ )
21   |   |   |  $L.\text{remove}(\text{ZZ}(\gamma[c, t]))$ 
22   |   | end
23   | end
24   | if  $L$  is empty then continue
25   | foreach  $(i, j) \in S[k]$  do
26   |   |  $c, t = O[i], O[j]$ 
27   |   | if  $c > t$  then
28   |   |   |  $c \leftrightarrow t$  // Exchange
29   |   | end
30   |   | if ZZ( $\gamma[c, t]$ ) in  $L$  then
31   |   |   | ApplyZZGate( $O, c, t$ )
32   |   |   |  $L.\text{remove}(\text{ZZ}(\gamma[c, t]))$ 
33   |   | if  $L$  is empty then continue
34   |   |   | ApplySWAPGate( $O, i, j$ )
35   | end
36 end
37 end
38 foreach SWAP on  $(i, j)$  located at the circuit end do
39   | Remove SWAP
40   |  $O[i] \leftrightarrow O[j]$ 
41 end
42 for  $k \leftarrow 0$  to  $n$  do
43   | Apply  $R_Z(\alpha[O[k]])$  on  $k$ 
44   | Apply  $R_X(\beta[O[k]])$  on  $k$ 
45 end
46 Measure the qubits  $([0, \dots, n-1] \rightarrow [O[0], \dots, O[n-1]])$ 

```

---

$(n_{\text{even}} - 2, n_{\text{even}})$ . For even numbers of qubits, the first and third layers are identical, which include connections between two center qubits. In contrast, the second and fourth layers differ in the first and last connections, where  $(1, 2)$  and  $(n_{\text{odd}} - 2, n_{\text{odd}} - 1)$  are for the second layer and  $(0, 2)$  and  $(n_{\text{odd}} - 2, n_{\text{odd}})$  are for the fourth layer. This

---

**Algorithm 4:** Swap layers on H-shaped subtopology

---

**Input:** Number of qubits  $n$

**Output:** List of swap layers  $S$

```

1 begin
2   |  $n_{\text{odd}} \leftarrow (n-1) - 1 + (n-1) \bmod 2$ ;
3   |  $n_{\text{even}} \leftarrow (n-1) - (n-1) \bmod 2$ ;
4   |  $S \leftarrow$  empty List;
5   |  $j \leftarrow 0$ ;
6   | if  $n \bmod 2 \neq 0$  then
7   |   | while  $j < n$  do
8   |   |   |  $S[j] \leftarrow$ 
9   |   |   |   |  $S[j] \cup [(0, 2), (3, 4), \dots, (n_{\text{odd}} - 2, n_{\text{odd}} - 1)]$ ;
10  |   |   | if  $++j \geq n$  then break;
11  |   |   |  $S[j] \leftarrow$ 
12  |   |   |   |  $S[j] \cup [(2, 3), (4, 5), \dots, (n_{\text{even}} - 2, n_{\text{even}} - 1)]$ ;
13  |   |   | if  $++j \geq n$  then break;
14  |   |   |  $S[j] \leftarrow$ 
15  |   |   |   |  $S[j] \cup [(2, 3), \dots, (n_{\text{even}} - 4, n_{\text{even}} - 3), (n_{\text{even}} - 2, n_{\text{even}})]$ ;
16  |   |   | if  $++j \geq n$  then break;
17  |   | end
18  | else
19  |   | while  $j < n$  do
20  |   |   |  $S[j] \leftarrow$ 
21  |   |   |   |  $S[j] \cup [(2, 3), (4, 5), \dots, (n_{\text{even}} - 2, n_{\text{even}} - 1)]$ ;
22  |   |   | if  $++j \geq n$  then break;
23  |   |   |  $S[j] \leftarrow$ 
24  |   |   |   |  $S[j] \cup [(1, 2), (3, 4), \dots, (n_{\text{odd}} - 2, n_{\text{odd}} - 1)]$ ;
25  |   |   | if  $++j \geq n$  then break;
26  |   |   |  $S[j] \leftarrow$ 
27  |   |   |   |  $S[j] \cup [(0, 2), \dots, (n_{\text{odd}} - 4, n_{\text{odd}} - 3), \dots, (n_{\text{odd}} - 2, n_{\text{odd}})]$ ;
28  |   |   | if  $++j \geq n$  then break;
29 end

```

---

alternating pattern of connections between neighboring swap layers efficiently constructs the set of minimized SWAP gates for VQAs with arbitrary numbers of qubits mapped to H-shaped topology.

The procedure to construct a depth-one circuit with arbitrary qubit number  $n$  on H-shaped subtopology is similar to Algorithm 3 for T-shaped subtopology. The list of connected edges  $E$  is updated to reflect the H-shaped connectivity, and the list of  $n$  swap layers  $S$  is generated according to Algorithm 4 for H-shaped subtopology. Similarly, repeating the same swap layers at depth  $p = 1$  circuit or leveraging mirror symmetry extends solutions to high depths. Compared to linear and T-shaped topologies, H-shaped topology enables additional connections for two center qubits that reduce required SWAP gates but increase circuit depth.

TABLE II. Hellinger distance between original and mapped circuits with AOQMAP-L using QAOA at a depth ranging from 1 to 7.

$p$	1	2	3	4	5	6	7
3-qubit	0.0045	0.0036	0.0033	0.005	0.0036	0.0048	0.0051
4-qubit	0.0044	0.0064	0.0057	0.0051	0.005	0.006	0.0044
5-qubit	0.0087	0.0067	0.0086	0.0103	0.0072	0.0095	0.0071
6-qubit	0.0138	0.0117	0.0138	0.0102	0.0123	0.0131	0.0124
10-qubit	0.0120	0.0127	0.0137	0.0127	0.0106	0.0158	0.0123

#### 4. Verification of circuits

After obtaining routing solutions on various subtopologies, the circuit is decomposed into basis gates of target QPUs, followed by an optimization step aiming to reduce redundant gates in circuit and improve fidelity. This decomposition and optimization process is performed using Qiskit transpiler [25] with default settings (optimization level 1). To maintain effectiveness, it is necessary to enforce the same or reduced number of CX gates during decomposition and optimization. Moreover, we verify the accuracy of adapted circuit by comparing output probability distributions of adapted and original circuits with Hellinger distance [46], which ranges from 0 to 1, with 0 indicating identical distributions. The Hellinger distance of two probability distributions is given by

$$H(P, Q) = (1 - \sum_j \sqrt{p_j q_j})^{1/2}, \quad (4)$$

where  $p_j$  and  $q_j$  are probabilities of outcome  $j$  in distributions  $P$  and  $Q$ , respectively. The verification process begins by simulating each circuit using a quantum simulator to obtain the expected output state in the absence of noise. In this study, we employ the QASM simulator provided by Qiskit to execute original and mapped circuits. We then calculate the Hellinger distance between probability distributions of simulated output states.

Table II reports the Hellinger distance between original and mapped circuits generated using AOQMAP on linear subtopology (AOQMAP-L). The benchmark circuits are QAOA for portfolio optimization with 3, 4, 5, 6, and 10 qubits and depths ranging from 1 to 7. Each data point is averaged over 50 circuit repetitions, with a standard error of the means that is more than 15 orders of magnitude smaller than the mean. The Hellinger distance increases with qubit number but remains two orders of magnitude smaller than one. Values greater than 0 are due to measurement noise or shot noise generated when executing circuits using the QASM simulator. This observation confirms that the mapped circuits are consistent with the originals across the problem instances studied.

#### B. Mapping of subtopology-adapted circuits

The next crucial step is to map these subtopology-aware circuits onto target quantum device by selecting an optimal qubit mapping scheme. To identify a high-quality qubit set, we utilize a cost function denoted as  $C$ , which takes into account the error rate of each gate and measurement in the circuit and is given by

$$C = 1 - \prod_{i=1}^{N_g} (1 - p_{g_i}) \prod_{j=1}^{N_m} (1 - p_{m_j}), \quad (5)$$

where  $N_g$  is number of gates in circuit,  $p_{g_i}$  is error rate of the  $i$ th gate,  $N_m$  is number of measurements, and  $p_{m_j}$  is error rate of the  $j$ th measurement. A lower value of  $C$  indicates a higher estimated fidelity. The error rates of gates and measurements can be obtained from device calibration data. To select optimal qubits, we first utilize mapomatic [41] to identify all layouts on QPU matching connectivity of adapted circuit. We evaluate circuit on each layout, choosing the one with the highest fidelity for execution. Since IBM QPUs like Fig. 1 contain more linear and T-shaped subtopologies than H-shaped, we focus on mapping to linear and T-shaped in our demonstrations. Additionally, H-shaped subtopologies on IBM QPUs are limited to specific qubit numbers such as 7, 9, 11, 13, and 15, whereas linear and T-shaped provide more flexibility.

We adopt a postselection process to determine between linear and T-shaped mappings instead of relying solely on cost function evaluation. Specifically, we execute circuits on both subtopologies and use postselection to select the circuit corresponding to the minimum expectation value of the problem Hamiltonian. While fidelity estimates from the cost function are valuable, factors such as gate scheduling can also impact algorithm performance [43]. Moreover, different gate arrangements may be equivalent in the absence of noise but behave differently under actual hardware noise. Therefore, we further introduce an additional variant called AOQMAP-LS which performs AOQMAP on linear subtopology with mirror symmetric swap layers in depth  $p = 1$ .

#### C. Optimality and scalability

The optimal swap strategy on line topology with  $n$  qubits has been proven to necessitate  $n - 2$  total swap layers to achieve fully connected two qubit gates [23]. This paper utilizes an exact method to obtain optimal solutions for small scale instances. By repeating swap layers or utilizing their symmetry, these solutions can be extended to any depth  $p$ . The analysis of these solutions allows for scalability in terms of the number of qubits. Similarly, we are able to obtain solutions for T- and H-shaped topologies for VQAs with arbitrary depths and numbers of qubits. For Hamiltonian with partially connected two-qubit interactions, scalability in terms of

depths is maintained through mirror symmetry. However, in terms of qubit numbers, we need to optimize the initial qubit mapping to minimize CX gate count, which we discuss in Sec. IV A.

To compare scalability, we measure compilation time to obtain optimal mappings that minimize circuit depth using an exact approach proposed in Ref. [16]. The original work on the compiler in Ref. [16] focused on an entire topology rather than a specific substructure. Therefore, we map QAOA circuits onto the entire topology of a 27-qubit IBM QPU, as depicted in Fig. 1. For three-qubit QAOA circuits, the compilation time of an exact algorithm increases exponentially with higher depth  $p$ , expanding from seconds at depth 1 to over 5 days at depth 7. Similarly, four-qubit compilation requires 13 seconds for depth 1 but grows substantially to over 15 hours for depth 2 and more than a week for depth 3. Furthermore, increasing qubit number from 3 to 9 lengthens compilation from 3 seconds to over 41 hours. In contrast, our approach intrinsically generalizes solutions for arbitrary depth and number of qubits without computation efforts. Specifically, we offer optimal and scalable solutions for Hamiltonian with fully connected interactions on linear, T-, and H-shaped subtopologies. We employ exact methods to attain optimality for small instances and use analytical techniques to extend these solutions to larger instances, thereby achieving scalability. This approach opens up the possibility of obtaining optimal and scalable solutions for specific problems.

## IV. APPLICATIONS

### A. QAOA for MaxCut on noncomplete graphs

QAOA is a VQA designed specifically to address combinatorial optimization problems, such as the MaxCut problem for graphs [3]. This problem involves partitioning nodes of a graph into two distinct groups to maximize the number of edges that connect these groups [47]. The problem Hamiltonian in QAOA for MaxCut problem is represented as

$$H_p = \frac{1}{2} \sum_{i,j} (1 - Z_i Z_j), \quad (6)$$

where  $i$  and  $j$  are two nodes of an edge. Compared to QAOA for portfolio optimization (Eq. 1), QAOA for the MaxCut problem does not include Pauli  $Z$  items, implying the absence of  $R_Z$  gates in quantum circuit. QAOA for MaxCut starts with state preparation and then alternately applies the problem and mixer Hamiltonian to evolve the state toward an optimal solution. QAOA for MaxCut problem on complete graphs follows a similar approach to QAOA for portfolio optimization. However, in noncomplete graphs, the lack of connectivity necessitates the exclusion of corresponding ZZ gates, introducing additional challenges for qubit mapping.

For VQAs with partially connected two-qubit gates, swap layers obtained from fully connected interactions can still ensure that the circuit satisfies connectivity constraints. In such cases, ZZ-SWAP gate corresponding to the missing edge is replaced by a SWAP gate, allowing for correct execution of quantum circuits on subtopologies. However, the presence of remaining SWAP gates due to the lack of two-qubit interactions significantly amplifies errors caused by noise. One solution is to optimize initial mapping or initial qubit order such that all SWAP gates are placed at the end of circuit. These end-located SWAP gates can then be removed by adjusting measurement order accordingly. Furthermore, if a SWAP gate is placed behind a ZZ gate in the first ZZ layer, it can be removed by adjusting the initial qubit order since ZZ and SWAP gates commute.

Algorithm 5 presents pseudocode for mapping QAOA for MaxCut on noncomplete graphs by optimizing initial qubit order. For  $n$  qubits, there are  $n!/2$  distinguished permutations due to symmetry. Different initial qubit orders introduce different gate arrangements, resulting in different numbers of CX gates. By minimizing additional CX gates, we can obtain an optimized qubit mapping. Practically, we can calculate the optimal or minimum number of CX gates in the resulting circuit. This optimal solution arranges all existing ZZ gates in consecutive layers until all gates are implemented. Then, we remove every SWAP gate behind the first ZZ layer and the one located at the end of circuit. This yields solutions with the minimum number of CX gates. To accelerate the search process, we can set the calculated optimal CX gate count as a target and terminate optimization once an initial qubit order achieves this value. It's important to note that the optimal initial order is not unique. Alternatively, we can employ a heuristic approach, where a certain size of initial qubit orders is searched, and the one with the fewest number of CX gates is selected [48]. For higher depth, we can obtain the solution by utilizing mirror symmetry, which involves alternating between swap layers at depth  $p = 1$  and their corresponding mirrors, resulting in a circuit repeating every two depths.

### B. Variational quantum eigensolver

In the previous section, we presented optimal routing solutions for QAOA on different types of subtopologies, including linear, T-, and H-shaped. One notable advantage of our approach is its applicability to other VQAs, such as VQE, without requiring additional computational resources. This is because both VQAs involve sequences of parameterized single qubit rotations and fixed two qubit operations. Therefore, optimal qubit routing solutions that we derived for QAOA based on subtopology connectivities can be easily adapted.

VQE [49–51] is designed to determine the ground state energy or eigenvalue of a Hamiltonian. It has broad applications in various fields such as quantum chemistry [52],

**Algorithm 5:** AOQMAP for QAOA at depth  $p = 1$  with partially connected ZZ interactions

---

**Input:** Number of qubits  $n$ , Parameters  $\gamma[c, t]$  and  $\beta[j]$  of gates ZZ on qubit pair  $(c, t)$  and Rx on qubit  $j$ , respectively, where  $c, t, j \in \{0, \dots, n-1\}$  and  $c < t$

**Output:** Circuit satisfying connectivity constraints

- 1  $O \leftarrow \{0, 1, \dots, n-1\}$  // Initialize the qubit order
- 2  $\mathcal{O}_q \leftarrow$  List of defined qubit orders
- 3  $L \leftarrow$  List of all existing ZZ gates
- 4 **Function**  $\text{MapTwoQubitGates}(O, L, \gamma)$
- 5    $O_0 \leftarrow O$  // Initial qubit order
- 6   **foreach** ZZ in  $L$  **do**
- 7     Assign ZZ( $\gamma[c, t]$ ) according to  $O_0$  and swap layers obtained for fully connected two qubit interactions and update current qubit order  $O$  if SWAP is applied
- 8   **end**
- 9    $O_f \leftarrow O$  // Final qubit order
- 10   **foreach** SWAP on  $(i, j)$  located at the circuit end **do**
- 11     Remove SWAP
- 12      $O_f[i] \leftrightarrow O_f[j]$
- 13   **end**
- 14   **foreach** SWAP on  $(i, j)$  located at the end of first ZZ layer **do**
- 15     Remove SWAP
- 16      $O_0[i] \leftrightarrow O_0[j]$
- 17   **end**
- 18   **return**  $(qc_{zz}, O_f)$
- 19    $(qc_{zz}^{\text{opt}}, O_f) = \text{MapTwoQubitGates}(O, L)$
- 20    $n_{\text{cx}}^{\text{opt}} \leftarrow$  CX gate count of  $qc_{zz}^{\text{opt}}$
- 21   **for**  $O_i$  in  $\mathcal{O}_q$  **do**
- 22      $(qc_{zz}, O_{f_i}) = \text{MapTwoQubitGates}(O_i, L)$
- 23      $n_{\text{cx}} \leftarrow$  CX gate count of  $qc_{zz}$
- 24     **if**  $n_{\text{cx}} < n_{\text{cx}}^{\text{opt}}$  **then**
- 25        $n_{\text{cx}}^{\text{opt}} = n_{\text{cx}}$
- 26        $qc_{zz}^{\text{opt}} = qc_{zz}$
- 27        $O_f = O_{f_i}$
- 28     **end**
- 29 **end**
- 30 Apply  $H^{\otimes n}$
- 31 Apply  $qc_{zz}^{\text{opt}}$
- 32 **for**  $k \leftarrow 0$  **to**  $n$  **do**
- 33   | Apply Rx( $\beta[O_f[k]]$ ) on  $k$
- 34 **end**
- 35 Measure the qubits  $([0, \dots, n-1] \rightarrow [O_f[0], \dots, O_f[n-1]])$

---

condensed matter physics [53], and combinatorial optimization [54]. Let  $H$  be the Hamiltonian of a quantum system, and  $|\psi\rangle$  a trial wavefunction. The Rayleigh-Ritz quotient is bounded below by the ground state energy  $E_0$

$$E_0 \leq \frac{\langle \psi | H | \psi \rangle}{\langle \psi | \psi \rangle}. \quad (7)$$

The objective is to determine a quantum state by examining a parameterized ansatz state, denoted as  $|\psi(\theta)\rangle = U(\theta)|0\rangle$ , to minimize expectation value of Hamiltonian.

Here,  $|0\rangle$  represents initial state, and  $U(\theta)$  is the vector of parameters  $\theta$ , also known as variational form or ansatz, which represents a parameterized unitary transformation achievable through quantum circuit. The selection of ansatz circuits plays a critical role in determining the efficacy of VQE. Three prominent categories of ansatz circuits include chemically inspired [55], hardware-efficient ansatz (HEA) [34], and Hamiltonian variational [56].

In this study, we examine VQE with full entanglement, as demonstrated in previous research (e.g., [57]). The ansatz circuit begins with a layer of parameterized  $R_Y$  gates, followed by controlled-Z (CZ) gates that serve as entangling gates. Unlike CX gate, which distinguishes between control and target qubits, CZ gate is undirected. After that, another set of parameterized  $R_Y$  gates is performed, succeeded by measurement. For higher  $p$ , the subcircuit between the first layer and measurement is repeated  $p$  times. The circuit with  $n$  qubits and depth  $p$  contains  $(p+1)n$  parameters that require optimization by a classical optimizer. The full entanglement is achieved through  $n(n-1)/2$  CZ gates, each comprising one CX and two Hadamard gates.

Algorithm 6 describes procedure of AOQMAP for VQE with full entanglement on linear subtopology. It differs from Algorithm 1 in the gates used. We initiate the implementation of CZ gate with one CX and two Hadamard gates that act on the physical qubit representing target qubit of CX gate. Subsequently, we perform CZ-SWAP gate by inserting a SWAP gate after CX gate and the second Hadamard gate on the physical qubit representing control qubit of CX instead of target qubit, since the introduced SWAP gate alters qubit order. Analogously, we construct  $n-2$  swap layers for  $n$  qubits on linear subtopology, meaning that CZ gates are performed on the first and last layers, while the constructed CZ-SWAP gates are implemented on remaining layers. Finally,  $R_Y$  gates are assigned accordingly, followed by measurement. The qubit mapping solution for VQE circuits on T- and H-shaped subtopologies can be attained similarly. Additionally, Algorithm 5 can be employed to obtain solutions for non-fully entangled VQE. The mapped circuit with depth  $p = 1$  on five qubits is depicted in Fig. 7. Each SWAP gate introduces a new qubit order and adds one additional CX gate, resulting in a total of  $p(n-1)^2$  CX gates. The incorporated SWAP gates guarantee that all requisite CZ gates can be executed.  $R_Y$  gates and measurement operators are then assigned according to the current qubit order.

The AOQMAP approach offers several advantages. First, solutions for different subtopologies can be easily adapted between VQAs. This means that once solutions are found for a specific algorithm on target subtopology, they can be applied to other VQAs. Second, AOQMAP facilitates individual block optimization. For instance, the optimization of CZ-SWAP gate can be achieved by rearranging SWAP gate before the second Hadamard gate, while altering the qubit that Hadamard gate acts upon. Moreover, this structure allows for efficient pulse opti-

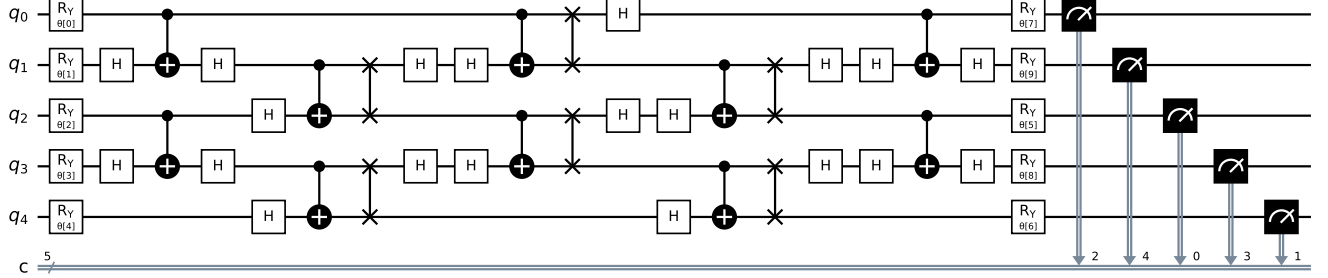


FIG. 7. Resulting circuit of a five-qubit VQE at depth  $p = 1$  with full entanglement on a linear subtopology using AOQMAP. The circuit can be further optimized by canceling two Hadamard gates and performing CX gate cancellation for CX-SWAP gates.

mization, as demonstrated in Ref. [43].

### C. Additional near-term quantum devices

AOQMAP offers versatility in optimizing algorithms on various NISQ devices. This adaptability is achieved by a decomposition-optimization-remapping workflow, where the circuit is first decomposed into basis gates of target device, then optimized, and finally mapped onto target topology, taking into account the latest device calibration data. This approach is particularly effective for square lattice qubit connectivity. For instance, Google’s Sycamore processor [58] provides more opportunities for linear, T-, and H-shaped qubit subtopologies within lattice. An H-shaped subtopology can readily materialize in the processor by identifying two neighboring square faces in the grid and their linear connection. Similarly, solutions can be suitably mapped to Rigetti’s processor [59] based on its noise characteristics. This exemplifies the applicability of AOQMAP to various QPUs with assorted connectivities. AOQMAP facilitates the transfer of solutions among diverse quantum devices, taking into account each specific architecture and noise information. As novel architectures proliferate, AOQMAP’s customized adaptability enables algorithms to be easily adjusted. This flexibility stands as a crucial advantage of AOQMAP in the era of NISQ computing.

## V. BENCHMARKING EXPERIMENTS

In this section, we present benchmarking results of QAOA for portfolio optimization problems on several IBM QPUs. We evaluate the efficiency of our method against three other approaches: Qiskit [25], Tket [26], and SWAP network (SWAPNK) [20].

Table III summarizes the characteristics of IBM QPUs employed in our benchmarking experiments. It is worth noting that these characteristics fluctuate over time. The processors used in our study range from 7 to 127 qubits.

The native gate set on 7- and 27-qubit QPUs is  $\{\text{CX}, \text{ID}, \text{R}_Z, \text{SX}, \text{X}\}$ , comprising CX, identity gate, single-qubit Z-rotation,  $\pi/2$  X-rotation, and Pauli-X. The 127-qubit QPUs implement a basis set of  $\{\text{ECR}, \text{ID}, \text{R}_Z, \text{SX}, \text{X}\}$ , where ECR is echoed cross-resonance two-qubit gate. The average error rate for single qubit gates varies from  $10^{-4}$  to  $10^{-2}$ , while for two-qubit gates, it is typically an order of magnitude higher, around  $10^{-2}$ . Additionally, average readout error rates are approximately  $10^{-2}$ . The average gate lengths for single-qubit gates range from 32 ns to 60 ns, whereas for two-qubit gates, they range from 306.96 ns to 665.83 ns. Furthermore, the mean energy relaxation time  $T_1$  ranges from 101.06  $\mu$ s to 227.95  $\mu$ s across different processors, and the average dephasing time  $T_2$  ranges from 71.04  $\mu$ s to 166.11  $\mu$ s. These comprehensive devices allow us to validate our optimization techniques across various qubit numbers, connectivity options, and noise properties.

The portfolio optimization instances utilized in this study are obtained from the supplementary information of Ref. [42]. Five different problem sizes are examined, involving the selection of the first 3, 4, 5, 6, and 10 assets from the portfolio optimization dataset. In QAOA, the key parameters  $(q, B, A, \lambda)$  vary depending on problem size. Here,  $q$ ,  $B$ ,  $A$ , and  $\lambda$  respectively represent risk preference, number of assets to be selected for the portfolio, penalty factor, and global scaling factor. The parameter values  $(q, B, A, \lambda)$  for each case are as follows:  $(0.33, 2, 0, 20.97)$  for three-qubit,  $(0.33, 2, 0.13, 17.99)$  for four-qubit,  $(0.33, 3, 0.07, 17.51)$  for five-qubit,  $(0.33, 3, 0.12, 17.73)$  for six-qubit, and  $(0.33, 5, 0.05, 6)$  for ten-qubit scenario.

### A. Evaluation metrics

We utilize circuit metrics including CX gate count and circuit depth to evaluate various qubit mapping methods. Additionally, we employ approximation ratio (AR) and success probability (SP) to assess the performance of QAOA.

---

**Algorithm 6:** AOQMAP for VQE on linear subtopology

---

**Input:** Number of qubits  $n$ , VQE depth  $p$ , Vector of parameters  $\theta$  with dimension  $(p+1) \times n$   
**Output:** Circuit satisfying connectivity constraints

```

1 Function ApplyCZGate( $i, j$ )
2   | Apply H on  $j$ 
3   | Apply CX on  $(i, j)$ 
4   | Apply H on  $j$ 
5 end
6 Function ApplyCZSWAPGate( $O, i, j$ )
7   | Apply H on  $j$ 
8   | Apply CX on  $(i, j)$ 
9   | Apply SWAP on  $(i, j)$ 
10  |  $O[i] \leftrightarrow O[j]$  // Exchange qubit order
11  | Apply H on  $i$ 
12 end
13  $O \leftarrow \{0, 1, \dots, n-1\}$  // Initialize the qubit order
14 Prepare the initial state  $|0\rangle^{\otimes n}$ 
15 for  $i := 0$  to  $n$  do
16   | Apply  $Ry(\theta[i])$  on  $i$ 
17 end
18  $p_{\max} \leftarrow p$ 
19 while  $p > 0$  do
20    $s \leftarrow 0$ 
21   while  $s < n$  do
22     for  $q := 0$  to  $n-1$  step 2 do
23       if  $s == 0$  or  $s == n-1$  then
24         | ApplyCZGate( $q, q+1$ )
25       else
26         | ApplyCZSWAPGate( $O, q, q+1$ )
27       end
28     end
29      $s \leftarrow s + 1$ 
30     if  $s < n$  then
31       for  $q := 1$  to  $n-1$  step 2 do
32         if  $s == 0$  or  $s == n-1$  then
33           | ApplyCZGate( $q, q+1$ )
34         else
35           | ApplyCZSWAPGate( $O, q, q+1$ )
36         end
37       end
38     end
39   end
40   for  $i := 0$  to  $n$  do
41     | Apply  $Ry(\theta[i + n(p_{\max} - p + 1)])$  on  $O[i]$ 
42   end
43    $p \leftarrow p - 1$ 
44 end
45 Measure the qubits  $([0, \dots, n-1] \rightarrow [O[0], \dots, O[n-1]])$ 

```

---

Portfolio optimization refers to the process of maximizing returns while minimizing risk by selecting a subset of  $n$  assets ( $n$  qubits). Generally, a defined number of assets needs to be selected, which is called the budget constraint. If the solution violates the budget constraint, the value of AR is defined as 0, otherwise it is defined as

$$r = \frac{F - F_{\max}}{F_{\text{opt}} - F_{\max}}, \quad (8)$$

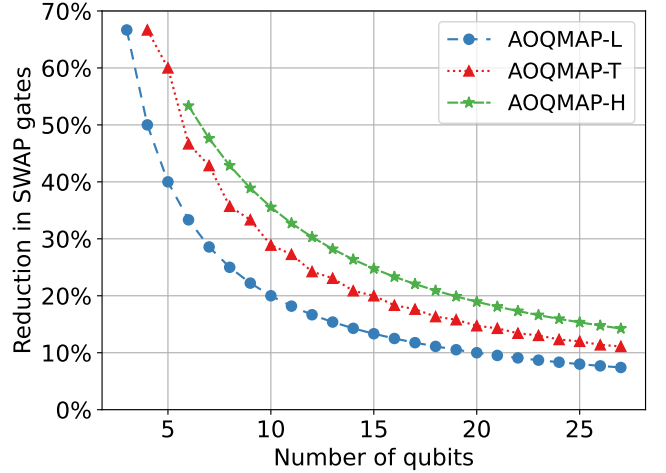


FIG. 8. Reduction in the number of SWAP gates for QAOA with depth  $p = 1$  using AOQMAP-L, AOQMAP-T, and AOQMAP-H compared to SWAPNK.

where  $F$ ,  $F_{\text{opt}}$ , and  $F_{\max}$  are the average value found by QAOA, the optimal/minimum value, and the worst-case/maximum value, respectively. The SP is defined as the probability of obtaining an optimal solution. A higher value of AR or SP implies a more effective algorithm performance, while a lower value of CX gate count or circuit depth indicates a high quality of the qubit mapping solution.

## B. Comparison of qubit mapping strategies

To ensure fair benchmarking, we employ various qubit mapping techniques to map circuits onto target quantum hardware, followed by decomposing and optimizing these circuits using Qiskit [25] with default settings (optimization level 1). For Tket [26], we employ NoiseAwarePlacement to select the lowest-noise qubits based on target QPUs' noise properties. The default Tket routing method *RoutingPass* is employed to insert SWAP gates. For Qiskit [25], we transpile with default settings. Finally, to map SWAPNK [20], we apply the same mapping strategy as AOQMAP, as detailed in Sec. III B.

### 1. Circuit properties

We first compare our approach with SWAPNK [20]. Figure 8 presents the reduction in SWAP gates for QAOA at depth  $p = 1$  using AOQMAP on linear (AOQMAP-L), T- (AOQMAP-T), and H-shaped (AOQMAP-H) subtopologies compared to SWAPNK. Specifically, AOQMAP-L leads to a decrease of 67% in SWAP gates for three-qubit and 20% for ten-qubit. Moreover, AOQMAP-T reduces SWAP gates by 67% for four-qubit and 29% for ten-qubit, whereas AOQMAP-H

TABLE III. Characterization of IBM QPUs.

Property	ibm_perth	ibm_nairobi	ibmq_ehning	ibmq_kaolkata	ibm_cusco	ibm_nazca
Qubit number	7	7	27	27	127	127
Single qubit gate error	4.867e-04	3.049e-04	3.348e-04	3.732e-02	2.703e-03	8.61e-04
Two qubit gate error	1.140e-02	8.749e-03	1.025e-02	1.855e-01	8.861e-02	5.49e-02
Readout error	2.443e-02	3.007e-02	1.230e-02	2.600e-02	5.509e-02	5.18e-02
Single qubit gate length	35.56 ns	35.56 ns	32.00 ns	35.56 ns	44.00 ns	60.00 ns
Two qubit gate length	485.93 ns	306.96 ns	346.98 ns	450.29 ns	487.22 ns	658.17 ns
$T_1$	162.06 $\mu$ s	101.06 $\mu$ s	143.82 $\mu$ s	103.18 $\mu$ s	131.51 $\mu$ s	197.66 $\mu$ s
$T_2$	123.82 $\mu$ s	71.04 $\mu$ s	166.11 $\mu$ s	82.98 $\mu$ s	109.17 $\mu$ s	128.56 $\mu$ s

TABLE IV. Reduction in CX or ECR gate counts of AOQMAP compared to other qubit mapping methods using QAOA with  $n$  qubits ( $nQ$ ) and depths from 1 to 7 on various IBM QPUs. Higher values indicate better performance of AOQMAP.

Benchmark	Tket	Qiskit	SWAPNK
3Q-Perth	(22%, 22%, 30%, 28%, 31%, 30%, 32%)	(22%, 22%, 30%, 28%, 31%, 30%, 32%)	(22%, 22%, 22%, 22%, 22%, 22%, 22%)
3Q-Kolkata	(22%, 22%, 30%, 28%, 31%, 30%, 32%)	(22%, 22%, 30%, 28%, 31%, 30%, 32%)	(22%, 22%, 22%, 22%, 22%, 22%, 22%)
3Q-Ehning	(22%, 22%, 30%, 28%, 31%, 30%, 32%)	(30%, 48%, 40%, 45%, 35%, 38%, 42%)	(22%, 22%, 22%, 22%, 22%, 22%, 22%)
3Q-Nairobi	(22%, 22%, 30%, 28%, 31%, 30%, 32%)	(22%, 22%, 30%, 28%, 31%, 30%, 32%)	(22%, 22%, 22%, 22%, 22%, 22%, 22%)
5Q-Perth	(10%, 28%, 28%, 30%, 30%, 31%, 31%)	(19%, 34%, 35%, 37%, 35%, 39%, 36%)	(13%, 20%, 20%, 20%, 20%, 20%, 20%)
5Q-Kolkata	(10%, 22%, 22%, 25%, 26%, 25%, 26%)	(21%, 29%, 30%, 32%, 32%, 34%, 34%)	(13%, 13%, 13%, 13%, 13%, 13%, 13%)
5Q-Cusco	(28%, 25%, 27%, 26%, 27%, 26%, 27%)	(32%, 34%, 38%, 38%, 38%, 39%, 39%)	(13%, 13%, 13%, 13%, 13%, 13%, 13%)
5Q-Ehning	(7%, 19%, 22%, 24%, 24%, 25%, 25%)	(48%, 50%, 54%, 52%, 53%, 56%, 53%)	(13%, 13%, 13%, 13%, 13%, 13%, 13%)
6Q-Ehning	(41%, 40%, 41%, 42%, 42%, 42%, 42%)	(39%, 43%, 45%, 43%, 44%, 44%, 45%)	(11%, 11%, 11%, 11%, 11%, 11%, 11%)
10Q-Kolkata	(52%, 50%, 48%, 52%, 53%, 48%, 54%)	(44%, 43%, 45%, 47%, 48%, 47%, 44%)	(10%, 7%, 7%, 7%, 7%, 7%, 10%)
10Q-Nazca	(48%, 53%, 55%, 55%, 56%, 56%, 56%)	(46%, 46%, 48%, 49%, 48%, 49%, 49%)	(7%, 7%, 7%, 7%, 7%, 7%, 7%)
10Q-Cusco	(51%, 53%, 55%, 55%, 56%, 56%, 56%)	(46%, 46%, 48%, 49%, 48%, 49%, 49%)	(7%, 7%, 7%, 7%, 7%, 7%, 7%)

TABLE V. Reduction in circuit depth. Same benchmarks as in Table IV.

Benchmark	Tket	Qiskit	SWAPNK
3Q-Perth	(30%, 21%, 29%, 25%, 29%, 26%, 29%)	(27%, 21%, 22%, 25%, 25%, 26%, 26%)	(10%, 11%, 11%, 11%, 11%, 11%, 11%)
3Q-Kolkata	(30%, 21%, 29%, 25%, 29%, 26%, 29%)	(27%, 21%, 22%, 25%, 25%, 26%, 26%)	(10%, 11%, 11%, 11%, 11%, 11%, 11%)
3Q-Ehning	(27%, 21%, 28%, 25%, 28%, 26%, 28%)	(14%, 28%, 22%, 26%, 19%, 22%, 25%)	(10%, 11%, 11%, 11%, 11%, 11%, 11%)
3Q-Nairobi	(30%, 21%, 29%, 25%, 29%, 26%, 29%)	(27%, 21%, 22%, 25%, 25%, 26%, 26%)	(10%, 11%, 11%, 11%, 11%, 11%, 11%)
5Q-Perth	(29%, 13%, 18%, 19%, 20%, 20%, 21%)	(43%, 23%, 27%, 34%, 28%, 36%, 28%)	(7%, -26%, -27%, -27%, -27%, -27%, -27%)
5Q-Kolkata	(29%, 36%, 40%, 46%, 47%, 46%, 47%)	(47%, 43%, 51%, 50%, 48%, 54%, 53%)	(7%, 7%, 8%, 8%, 8%, 8%, 8%)
5Q-Cusco	(53%, 50%, 50%, 49%, 50%, 49%, 49%)	(48%, 47%, 48%, 52%, 50%, 52%, 52%)	(13%, 13%, 12%, 12%, 11%, 12%, 11%)
5Q-Ehning	(21%, 26%, 28%, 29%, 30%, 30%, 31%)	(51%, 55%, 57%, 57%, 59%, 57%)	(7%, 7%, 8%, 8%, 8%, 8%, 8%)
6Q-Ehning	(48%, 43%, 44%, 48%, 45%, 46%, 48%)	(44%, 45%, 50%, 50%, 47%, 49%, 49%)	(6%, 6%, 7%, 7%, 7%, 7%, 7%)
10Q-Kolkata	(57%, 69%, 65%, 71%, 71%, 66%, 59%)	(54%, 66%, 67%, 69%, 72%, 71%, 27%)	(-33%, 4%, 4%, 4%, 4%, 4%, -35%)
10Q-Nazca	(74%, 75%, 79%, 80%, 81%, 82%, 82%)	(71%, 71%, 52%, 72%, 71%, 76%, 74%)	(6%, 6%, 6%, 5%, 5%, 5%, 5%)
10Q-Cusco	(75%, 75%, 79%, 80%, 81%, 81%, 81%)	(71%, 71%, 52%, 71%, 76%, 74%)	(7%, 7%, 6%, 6%, 6%, 7%, 6%)

reduces SWAP gates by 53% for six-qubit and 36% for ten-qubit. For QAOA with depth  $p$ , the reduction in SWAP gate count achieved is  $p$  multiplied by the reduction attained at depth  $p = 1$ .

We then compare our approach with Tket, Qiskit, and SWAPNK on IBM QPUs. The examined QAOA has depths ranging from 1 to 7 and qubit numbers 3, 5, 6, and 10. Tables IV and V present the reduction in two-qubit gate counts (CX or ECR) and circuit depth, respectively, of mapped circuits generated by AOQMAP compared to other approaches across various QPUs. We note that the 127-qubit QPUs natively implement ECR gates instead of CX gates. The results demonstrate that AOQMAP leads to reductions in CX or ECR gates and/or circuit depth compared to other approaches. For three-qubit QAOA, the number of CX gates remains the same re-

duction for AOQMAP compared to Tket and SWAPNK since three qubits can only form a linear subtopology. The difference in reduction in Qiskit is due to the randomness of Qiskit's transpiler. However, for five-qubit QAOA with depths ranging from 2 to 7, AOQMAP exhibits a higher CX gate reduction but lower circuit depth reduction on ibm\_perth (5Q-Perth) than ibmq\_kolkata (5Q-Kolkata). The reason is that a circuit adapted to T-shaped subtopology yields a lower expectation value of problem Hamiltonian and is selected. This selection of T-shaped topology further reduces the number of CX gates, but also increases circuit depth. For six-qubit QAOA on ibmq\_ehning, AOQMAP uses only linear subtopology, which has the least number of CX gates and the shortest depths compared to others. A T-shaped subtopology is also selected in AOQMAP for ten-qubit QAOA on

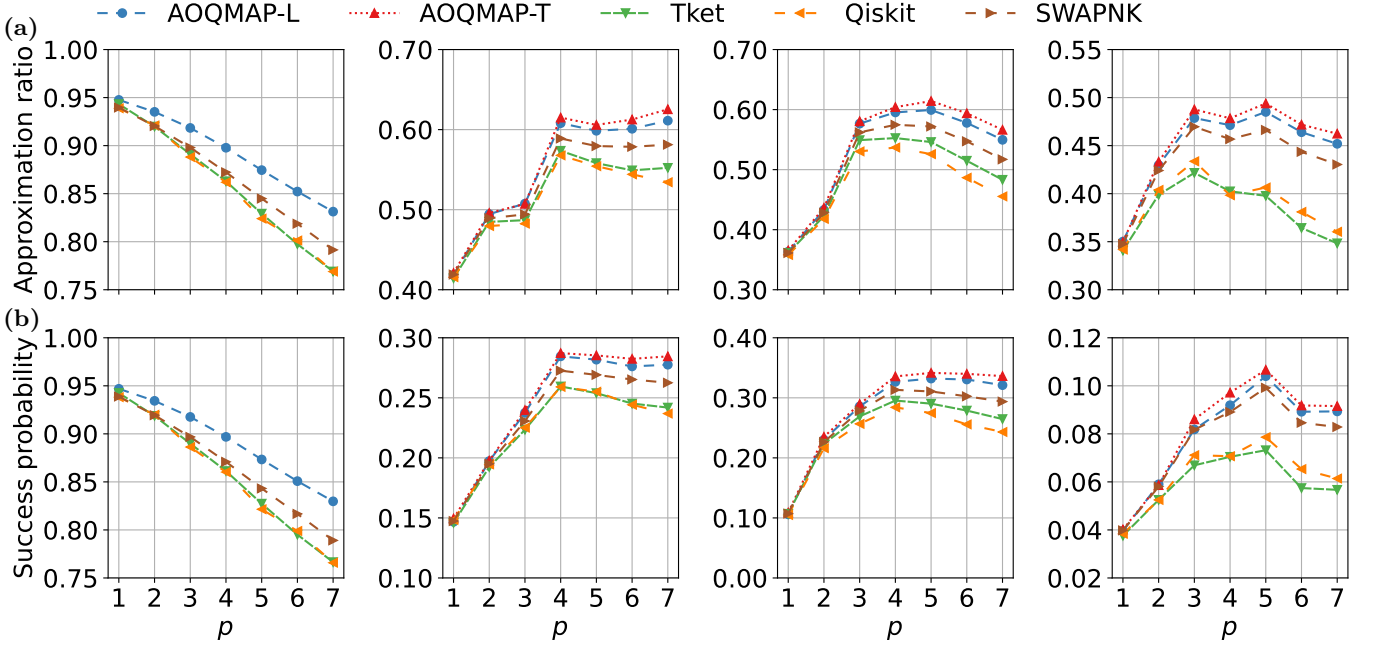


FIG. 9. Simulation under depolarizing noise of QAOA for portfolio optimization mapped with AOQMAP-L, AOQMAP-T, Tket, Qiskit, and SWAPNK. (a) Approximation ratio and (b) success probability for QAOA with three, four, five, and six qubits. Three-qubit QAOA has an absence of AOQMAP-T, as the minimum number of qubits required for the T-shaped subtopology is four.

ibmq\_kolkata at depths 1 and 7. The solutions provided by AOQMAP achieve the shortest circuit depth and/or the fewest number of CX or ECR gates compared to other approaches. Specifically, AOQMAP reduces two-qubit gate count by 29% (up to 56%) and circuit depth by 31% (up to 82%) on average compared to Qiskit, Tket, and SWAPNK.

## 2. Simulation under noise

To examine the impact of noise on the performance of QAOA with different qubit mapping strategies, we simulate algorithms mapped onto a 27-qubit QPU with the topology shown in Fig. 1. We use a depolarizing noise model [60, 61], which is a common simple model used to approximate the effects of mixed noise processes in quantum systems. This model captures noise effects by applying random single-qubit bit-flip, phase-flip, and combined bit- and phase-flip errors to each gate, providing a good approximation of the overall noise behavior and impact on algorithm performance. The depolarizing error channel, acting on qubits described by density matrix  $\rho$ , is defined as

$$E_D(\rho) = \frac{\epsilon}{4} (X\rho X + Y\rho Y + Z\rho Z) + (1 - \frac{3\epsilon}{4})\rho, \quad (9)$$

where  $X$ ,  $Y$ , and  $Z$  are Pauli matrices, and  $\epsilon$  is noise strength.

We compare AOQMAP-L and AOQMAP-T with Tket, Qiskit, and SWAPNK. The mapped circuits are simulated under depolarizing noise with strength 0.005 for two-qubit gates and  $\epsilon/10$  for single-qubit gates. Figure 9 presents the approximation ratio and success probability of QAOA on 3, 4, 5, and 6 qubits at depths from 1 to 7. Compared to other quantum mapping strategies, AOQMAP-L and AOQMAP-T demonstrate better performance at higher depths and comparable performance at depth  $p = 1$ . This suggests that increased depth of QAOA leads to a more significant noise effect, emphasizing advantages of AOQMAP. AOQMAP-T requires fewer CX gates during the mapping stage compared to others, which mitigates the detrimental effects of noise accumulation, leading to improved performance. For three-qubit QAOA, AR and SP decrease with increased depth, indicating that noise effects outweigh performance improvement at higher depths. In comparison, for QAOA with 4, 5, and 6 qubits, AR and SP increase and then stabilize or slightly decrease, suggesting a balance between performance improvements and noise effects.

## C. Demonstration on IBM quantum devices

We evaluate the performance of QAOA for portfolio optimization across six IBM QPUs, comparing different mapping approaches on 7-qubit ibm\_perth and ibm\_nairobi, 27-qubit ibmq\_kolkata and ibmq\_ehningen, and 127-qubit ibmq\_nazca and ibmq\_cusco. The problem

sizes QAOA include 3, 4, 5, 6, and 10 qubits, and depths ranging from 1 to 7.

As discussed in Sec. III A, two methods exist for constructing higher QAOA depth, including repeating swap layers in depth  $p = 1$  circuit and leveraging their symmetry. To examine the influence of symmetry, we conduct a comparative analysis of AOQMAP on linear subtopology with repetitive routing at depth  $p = 1$  (AOQMAP-L) and with mirror-symmetric swap layers (AOQMAP-LS), as well as AOQMAP on T-shaped subtopology (AOQMAP-T). We consider QAOA instances with four qubits and depths from 1 to 7. Figure 10 compares these variants to Tket, Qiskit, and SWAPNK on the 7-qubit `ibm_nairobi`. AOQMAP on linear subtopology utilizing symmetry significantly enhances the performance, increasing success probability by an average of 82% (up to  $1.83\times$ ) compared to AOQMAP-L, 76% (up to  $2.76\times$ ) compared to AOQMAP-T, 1.72× (up to  $3.80\times$ ) compared to Tket, 1.77× (up to  $3.21\times$ ) compared to Qiskit, and 73% (up to  $1.41\times$ ) compared to SWAPNK. These results demonstrate the effectiveness of symmetry for improving performance on NISQ devices, validating the advantage of AOQMAP’s symmetry-incorporated mapping approach.

For the demonstration on `ibmq_ehningen`, we directly compare AOQMAP-L with other methods, while for evaluations on other QPUs, a postselection process is utilized to generate the AOQMAP solution. Specifically, we construct the algorithms with AOQMAP-L, AOQMAP-LS, and AOQMAP-T. Each adapted circuit is mapped to the target device using the method described in Sec. III B. The demonstration solution corresponding to the minimum expectation value of the problem Hamiltonian is then chosen. As shown in Fig. 11(a), AOQMAP achieves the highest performance on all QPUs. Tket and Qiskit perform comparably on all QPUs, while SWAPNK performs better on `ibm_perth` and `ibmq_ehningen` than `ibm_kolkata` and `ibm_nairobi`. The approximation ratio decreases with increased depth, indicating that the negative impact of noise dominates the improved performance at higher depths. For five-qubit QAOA (Fig. 11(b)), AOQMAP maintains the highest AR across all QPUs. Tket outperforms Qiskit on `ibmq_kolkata` and `ibmq_ehningen`, whereas Qiskit performs better on `ibm_cusco`. SWAPNK has a better performance on `ibmq_perth` and `ibmq_kolkata`, while it performs worse on `ibmq_ehningen`. For six-qubit QAOA on `ibmq_ehningen`, AOQMAP has a significantly higher AR value than Tket, Qiskit, and SWAPNK (Fig. 11(c)). For the largest ten-qubit QAOA, AOQMAP consistently achieves the highest AR across all tested QPUs. SWAPNK has a higher AR only on `ibm_nazca`, while Qiskit and Tket perform worse on all QPUs. On `ibmq_kolkata`, AOQMAP achieves the highest AR value at depth two, outperforming others. With increased depth, the noise in large-scale circuit increases significantly, resulting in a reduced AR value. For ten-qubit QAOA on `ibm_cusco`, AOQMAP has the highest AR value at depth  $p = 1$ . The presence of the second-highest

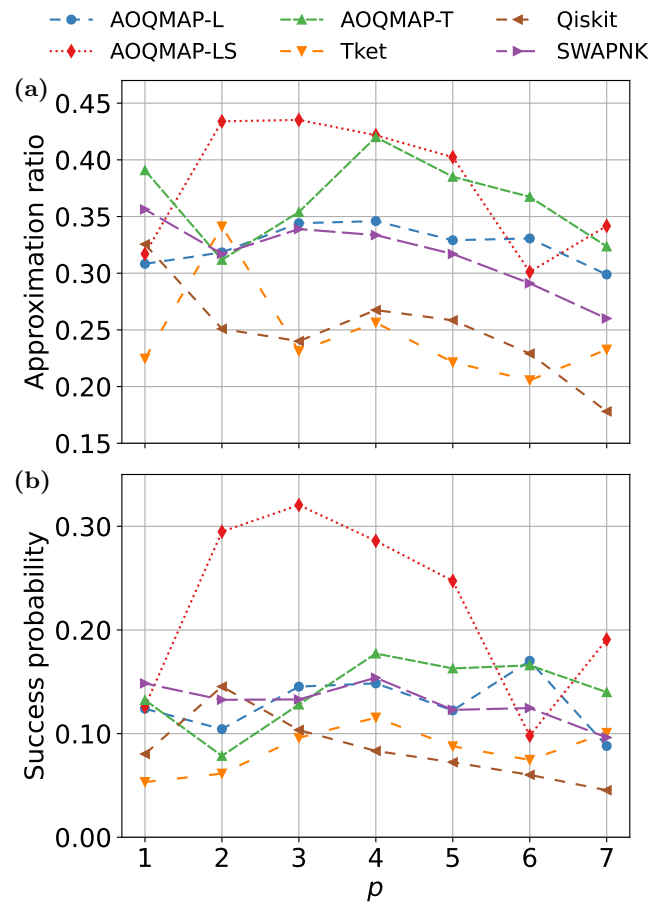


FIG. 10. Demonstration on 7-qubit QPU `ibm_nairobi`. (a) Approximation ratio and (b) success probability of four-qubit QAOA with depths ranging from one to seven using various qubit mapping methods.

AR at depth six demonstrates a trade-off between improved performance and introduced noise of the increased QAOA depth.

The success probability of QAOA with 3, 5, and 10 qubits (6 qubits for `ibmq_ehningen`) is displayed in Figs. 12(a-c), respectively, following a similar trend as the AR. AOQMAP demonstrates the highest SP overall with different circuit sizes across all QPUs. For QAOA with five and ten qubits, the SP initially increases with depth and then decreases, peaking at different  $p$  depending on device noise. This phenomenon indicates a balance between performance improvement and noise impact in high-depth circuits. For five-qubit QAOA, Qiskit performs better on `ibm_cusco`, Tket has higher performance on `ibmq_kolkata` and `ibmq_ehningen`, and SWAPNK has higher SP values on `ibmq_kolkata` and `ibm_cusco`. For ten-qubit QAOA, Tket and Qiskit have lower success probabilities on all QPUs, whereas SWAPNK performs better only on `ibm_nazca`.

These findings demonstrate that AOQMAP provides a significant improvement in approximation ratio and success probability, surpassing other popular qubit mapping

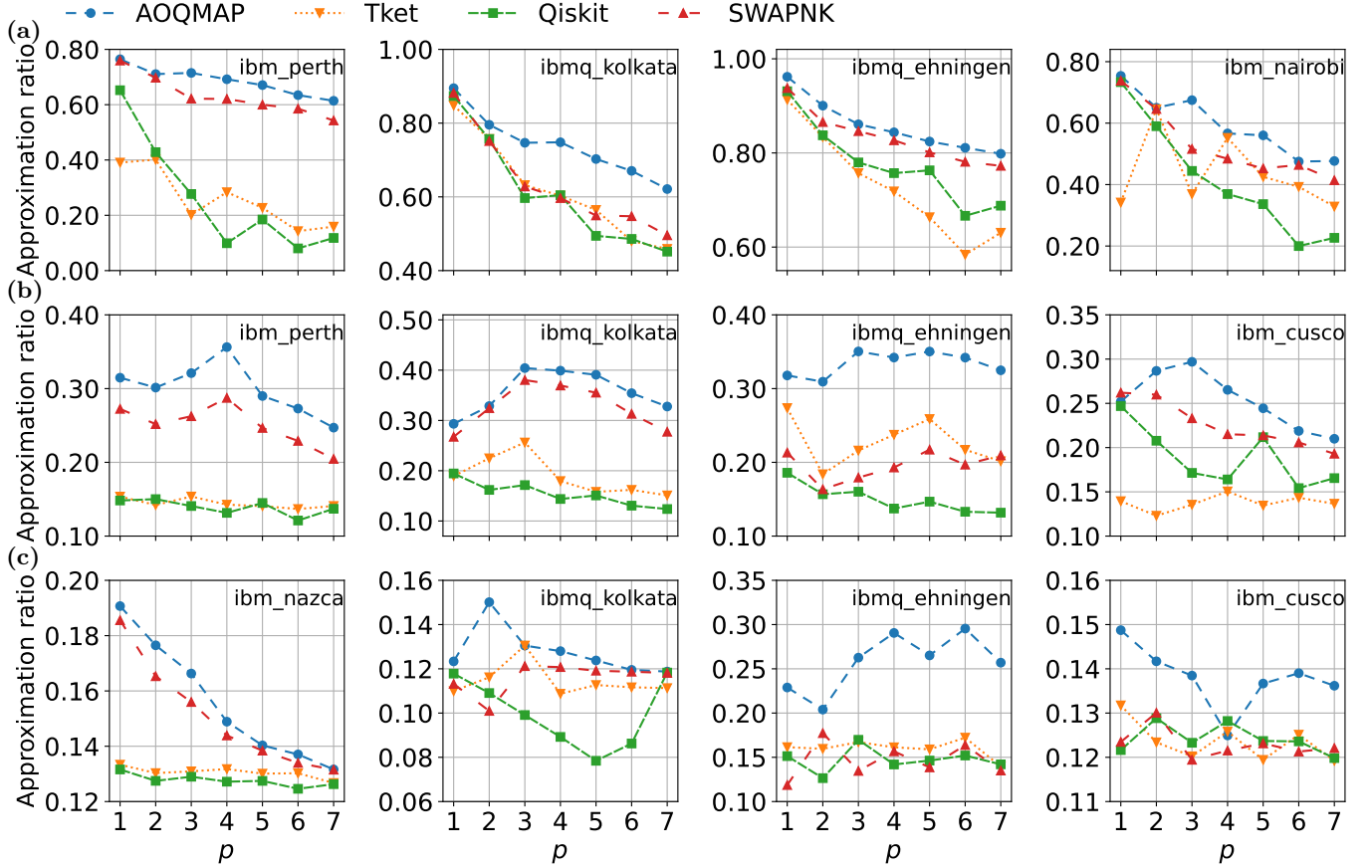


FIG. 11. Approximation ratio of QAOA obtained on various IBM QPUs using AOQMAP, Tket, Qiskit, and SWAPNK. The numbers of qubits are (a) three, (b) five, and (c) ten (six for ibmq\_ehningen). AOQMAP demonstrates the highest performance on all QPUs in comparison to other approaches.

approaches. In particular, AOQMAP improves AR by an average of 54% and SP by an average of 138% compared to Qiskit, Tket, and SWAPNK, demonstrating robust high performance on NISQ devices. Furthermore, our experiments on various QPUs highlight the limitations of solely relying on noise model simulations for assessing circuit performance. While such simulations provide valuable insights, they often fail to accurately capture the complex and multifaceted noise characteristics inherent to real quantum hardware. Although different qubit mapping strategies exhibit comparable behavior under simulated noise conditions, their performance diverges significantly when executed on physical devices. This disparity emphasizes the critical role of efficient qubit mapping in achieving high algorithm performance on NISQ devices.

## VI. CONCLUSION

We present an efficient qubit mapping methodology designed for VQAs on near term quantum devices. The method involves two essential steps: adapting circuits to

subtopologies and mapping adapted circuits onto target QPU. In the adaptation step, optimal routing solutions with the shortest circuit depth are provided for diverse subtopologies, including linear, T-, and H-shaped configurations. These solutions inherently scale to arbitrary depths and numbers of qubits for algorithms characterized by fully connected two qubit interactions. For partially connected interactions, optimizing initial qubit order enables the derivation of optimal depth-one solutions. Leveraging mirror symmetry, these solutions can be extended to higher QAOA depths without additional computational overhead. In the mapping step, the adapted circuit is mapped onto target device, minimizing circuit error with a cost function. A postselection process is then employed to choose the optimal solution that minimizes the expectation value of problem Hamiltonian. Demonstrations of QAOA for portfolio optimization on six IBM QPUs with 7, 27, and 127 qubits exhibit improved performance of AOQMAP compared to existing methods. We also show that the symmetry used in the circuit structure can improve algorithm performance on QPUs. These results and solutions can be easily applied to other NISQ devices. Our qubit mapping strategy tailors mappings to

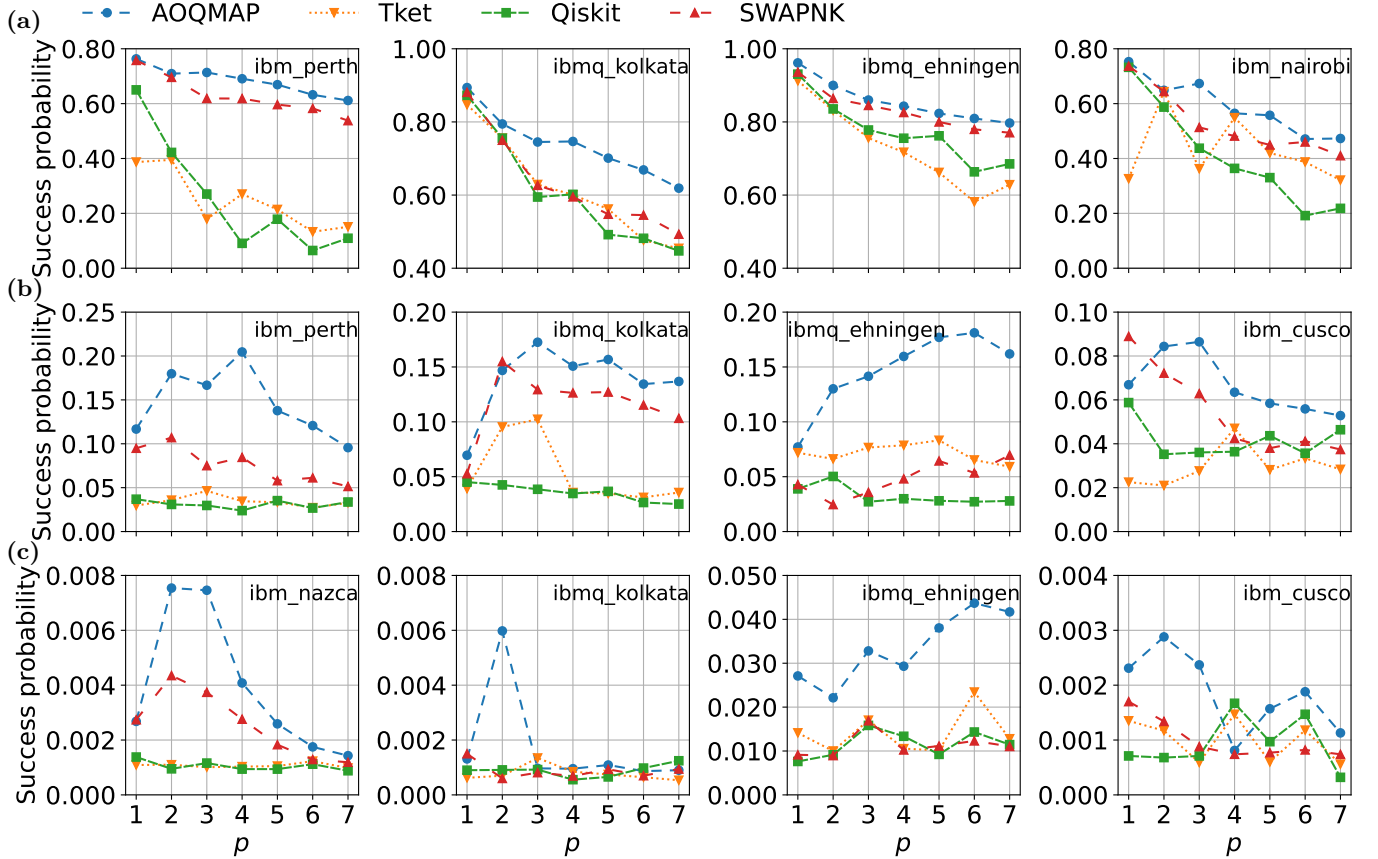


FIG. 12. Success probability of QAOA obtained on various QPUs with AOQMAP, Tket, Qiskit, and SWAPNK. The labels are the same as Fig. 11.

algorithmic structures, promising to maximize the capabilities of near term devices for VQAs.

Future research directions include extending our method to handle more complex topologies, such as T- and H-shaped variants, and heavy-hex. Furthermore, exploring strategies to adapt Hamiltonian with partially connected two-qubit gate interactions presents a promising avenue of exploration. While mirror symmetry of swap layers enables scaling solutions to high depths, the combinatorial complexity associated with the depth-one circuits remains a significant challenge. Developing heuristic optimization approaches to refine initial qubit mapping can accelerate the search process. The trade-off between computational cost and solution quality is essential for achieving efficient and effective optimization.

## ACKNOWLEDGMENTS

The authors would like to thank Kathrin F. Koenig, Thomas Wellens, Joris Kattemölle, Sebastian Brandhofer, Andreas Ketterer, Koushik Paul, Pranav Chandarana, Julián Ferreiro Vélez, and Pengcheng Zhu for

their useful discussions and exchanges. We acknowledge the use of IBM Quantum services for this work and to advanced services provided by the IBM Quantum Researchers Program. The views expressed are those of the authors, and do not reflect the official policy or position of IBM or the IBM Quantum team. The authors acknowledge the financial support of the project QORA by Ministerium für Wirtschaft, Arbeit und Tourismus Baden-Württemberg in the frame of the Competence Center Quantum Computing Baden-Württemberg, the Basque Government through Grant No. IT1470-22, the Project Grant No. PID2021-126273NB-I00 funded by MCIN/AEI/10.13039/501100011033 and by “ERDF A way of making Europe” and “ERDF Invest in your Future,” Nanoscale NMR and complex systems (Grant No. PID2021- 126694NB-C21), EU FET Open Grant EPIQUS (No. 899368), the ELKARTEK Program by the Basque Government under Grant KK-2022/00041, BRTA QUANTUM Hacia una especialización armonizada en tecnologías cuánticas en BRTA. X.C. acknowledges ayudas para contratos Ramón y Cajal-2015-2020 (Grant No. RYC-2017-22482) and open access funding provided by UPV/EHU.

[1] M. Cerezo, A. Arrasmith, R. Babbush, S. C. Benjamin, S. Endo, K. Fujii, J. R. McClean, K. Mitarai, X. Yuan, L. Cincio, *et al.*, Variational quantum algorithms, *Nature Reviews Physics* **3**, 625 (2021).

[2] K. Bharti, A. Cervera-Lierta, T. H. Kyaw, T. Haug, S. Alperin-Lea, A. Anand, M. Degroote, H. Heimonen, J. S. Kottmann, T. Menke, *et al.*, Noisy intermediate-scale quantum algorithms, *Reviews of Modern Physics* **94**, 015004 (2022).

[3] E. Farhi, J. Goldstone, and S. Gutmann, A quantum approximate optimization algorithm, arXiv preprint arXiv:1411.4028 (2014).

[4] H. Ma, M. Govoni, and G. Galli, Quantum simulations of materials on near-term quantum computers, *npj Computational Materials* **6**, 85 (2020).

[5] Y. Hu, F. Meng, X. Wang, T. Luan, Y. Fu, Z. Zhang, X. Zhang, and X. Yu, Greedy algorithm based circuit optimization for near-term quantum simulation, *Quantum Science and Technology* **7**, 045001 (2022).

[6] G. Li, Y. Ding, and Y. Xie, Tackling the qubit mapping problem for nisq-era quantum devices, in *Proceedings of the Twenty-Fourth International Conference on Architectural Support for Programming Languages and Operating Systems*, ASPLOS '19 (Association for Computing Machinery, New York, NY, USA, 2019) p. 1001–1014.

[7] A. Cowtan, S. Dilkes, R. Duncan, A. Krajenbrink, W. Simmons, and S. Sivarajah, On the Qubit Routing Problem, in *14th Conference on the Theory of Quantum Computation, Communication and Cryptography (TQC 2019)*, Leibniz International Proceedings in Informatics (LIPIcs), Vol. 135, edited by W. van Dam and L. Mancinska (Schloss Dagstuhl–Leibniz-Zentrum fuer Informatik, Dagstuhl, Germany, 2019) pp. 5:1–5:32.

[8] P. Zhu, S. Feng, and Z. Guan, An iterated local search methodology for the qubit mapping problem, *IEEE Transactions on Computer-Aided Design of Integrated Circuits and Systems* **41**, 2587 (2022).

[9] S. Niu, A. Suau, G. Staffelbach, and A. Todri-Sanial, A hardware-aware heuristic for the qubit mapping problem in the NISQ era, *IEEE Transactions on Quantum Engineering* **1**, 1 (2020).

[10] C. Zhang, A. B. Hayes, L. Qiu, Y. Jin, Y. Chen, and E. Z. Zhang, Time-optimal qubit mapping, in *Proceedings of the 26th ACM International Conference on Architectural Support for Programming Languages and Operating Systems*, ASPLOS '21 (Association for Computing Machinery, New York, NY, USA, 2021) p. 360–374.

[11] M. Y. Siraichi, V. F. d. Santos, C. Collange, and F. M. Q. Pereira, Qubit allocation, in *Proceedings of the 2018 International Symposium on Code Generation and Optimization*, CGO 2018 (Association for Computing Machinery, New York, NY, USA, 2018) p. 113–125.

[12] D. Bhattacharjee and A. Chattopadhyay, Depth-optimal quantum circuit placement for arbitrary topologies, arXiv preprint arXiv:1703.08540 (2017).

[13] A. Shafaei, M. Saeedi, and M. Pedram, Qubit placement to minimize communication overhead in 2d quantum architectures, in *2014 19th Asia and South Pacific Design Automation Conference (ASP-DAC)* (IEEE, 2014) pp. 495–500.

[14] P. Murali, J. M. Baker, A. Javadi-Abhari, F. T. Chong, and M. Martonosi, Noise-adaptive compiler mappings for noisy intermediate-scale quantum computers, in *Proceedings of the twenty-fourth international conference on architectural support for programming languages and operating systems* (2019) pp. 1015–1029.

[15] M. Y. Siraichi, V. F. d. Santos, C. Collange, and F. M. Q. Pereira, Qubit allocation as a combination of subgraph isomorphism and token swapping, *Proceedings of the ACM on Programming Languages* **3**, 1 (2019).

[16] B. Tan and J. Cong, Optimal layout synthesis for quantum computing, in *IEEE/ACM International Conference On Computer Aided Design, ICCAD 2020, San Diego, CA, USA, November 2-5, 2020* (IEEE, 2020) pp. 137:1–137:9.

[17] A. Zulehner, A. Paler, and R. Wille, An efficient methodology for mapping quantum circuits to the IBM QX architectures, *IEEE Transactions on Computer-Aided Design of Integrated Circuits and Systems* **38**, 1226 (2018).

[18] A. M. Childs, E. Schoute, and C. M. Unsal, Circuit Transformations for Quantum Architectures, in *14th Conference on the Theory of Quantum Computation, Communication and Cryptography (TQC 2019)*, Leibniz International Proceedings in Informatics (LIPIcs), Vol. 135, edited by W. van Dam and L. Mancinska (Schloss Dagstuhl–Leibniz-Zentrum fuer Informatik, Dagstuhl, Germany, 2019) pp. 3:1–3:24.

[19] Z.-T. Li, F.-X. Meng, Z.-C. Zhang, and X.-T. Yu, Qubits' mapping and routing for NISQ on variability of quantum gates, *Quantum Information Processing* **19**, 1 (2020).

[20] M. P. Harrigan, K. J. Sung, M. Neeley, K. J. Satzinger, F. Arute, K. Arya, J. Atalaya, J. C. Bardin, R. Barends, S. Boixo, *et al.*, Quantum approximate optimization of non-planar graph problems on a planar superconducting processor, *Nature Physics* **17**, 332 (2021).

[21] I. D. Kivlichan, J. McClean, N. Wiebe, C. Gidney, A. Aspuru-Guzik, G. K.-L. Chan, and R. Babbush, Quantum simulation of electronic structure with linear depth and connectivity, *Physical review letters* **120**, 110501 (2018).

[22] B. O'Gorman, W. J. Huggins, E. G. Rieffel, and K. B. Whaley, Generalized swap networks for near-term quantum computing, arXiv preprint arXiv:1905.05118 (2019).

[23] J. Weidenfeller, L. C. Valor, J. Gacon, C. Tornow, L. Bello, S. Woerner, and D. J. Egger, Scaling of the quantum approximate optimization algorithm on superconducting qubit based hardware, *Quantum* **6**, 870 (2022).

[24] A. Hashim, R. Rines, V. Omole, R. K. Naik, J. M. Kreikebaum, D. I. Santiago, F. T. Chong, I. Siddiqi, and P. Gokhale, Optimized swap networks with equivalent circuit averaging for qaoa, *Phys. Rev. Res.* **4**, 033028 (2022).

[25] IBM. 2022., IBM Qiskit, <https://qiskit.org/>, Accessed: 2022-10-31.

[26] S. Sivarajah, S. Dilkes, A. Cowtan, W. Simmons, A. Edgington, and R. Duncan,  $t\text{-ket}$ : a retargetable compiler for nisq devices, *Quantum Science and Technology* **6**, 014003 (2020).

[27] D. Rosenberg, S. J. Weber, D. Conway, D.-R. W. Yost, J. Mallek, G. Calusine, R. Das, D. Kim, M. E. Schwartz, W. Woods, J. L. Yoder, and W. D. Oliver, Solid-state

qubits: 3d integration and packaging, *IEEE Microwave Magazine* **21**, 72 (2020).

[28] B. M. Niedzielski, D. K. Kim, M. E. Schwartz, D. Rosenberg, G. Calusine, R. Das, A. J. Melville, J. Plant, L. Racz, J. L. Yoder, D. Ruth-Yost, and W. D. Oliver, Silicon hard-stop spacers for 3d integration of superconducting qubits, in *2019 IEEE International Electron Devices Meeting (IEDM)* (2019) pp. 31.3.1–31.3.4.

[29] J. Rahamim, T. Behrle, M. J. Peterer, A. Patterson, P. A. Spring, T. Tsunoda, R. Manenti, G. Tancredi, and P. J. Leek, Double-sided coaxial circuit QED with out-of-plane wiring, *Applied Physics Letters* **110**, 222602 (2017), [https://pubs.aip.org/aip/apl/article-pdf/doi/10.1063/1.4984299/14500580/222602\\_1\\_online.pdf](https://pubs.aip.org/aip/apl/article-pdf/doi/10.1063/1.4984299/14500580/222602_1_online.pdf).

[30] P. Wang, C.-Y. Luan, M. Qiao, M. Um, J. Zhang, Y. Wang, X. Yuan, M. Gu, J. Zhang, and K. Kim, Single ion qubit with estimated coherence time exceeding one hour, *Nature communications* **12**, 233 (2021).

[31] G. Brida, I. P. Degiovanni, M. Genovese, F. Piacentini, P. Traina, A. Della Frera, A. Tosi, A. Bahgat Shehata, C. Scarella, A. Gulinatti, M. Ghioni, S. V. Polyakov, A. Migdall, and A. Giudice, An extremely low-noise heralded single-photon source: A breakthrough for quantum technologies, *Applied Physics Letters* **101**, 221112 (2012), [https://pubs.aip.org/aip/apl/article-pdf/doi/10.1063/1.4768288/14259225/221112\\_1\\_online.pdf](https://pubs.aip.org/aip/apl/article-pdf/doi/10.1063/1.4768288/14259225/221112_1_online.pdf).

[32] J. Preskill, Quantum computing in the nisq era and beyond, *Quantum* **2**, 79 (2018).

[33] P. Chandarana, P. S. Vieites, N. N. Hegade, E. Solano, Y. Ban, and X. Chen, Meta-learning digitized-counterdiabatic quantum optimization, *Quantum Science and Technology* **8**, 045007 (2023).

[34] A. Kandala, A. Mezzacapo, K. Temme, M. Takita, M. Brink, J. M. Chow, and J. M. Gambetta, Hardware-efficient variational quantum eigensolver for small molecules and quantum magnets, *Nature* **549**, 242 (2017).

[35] Y. Ji, S. Brandhofer, and I. Polian, Calibration-aware transpilation for variational quantum optimization, in *2022 IEEE International Conference on Quantum Computing and Engineering (QCE)* (IEEE, 2022) pp. 204–214.

[36] P. Gokhale, A. Javadi-Abhari, N. Earnest, Y. Shi, and F. T. Chong, Optimized quantum compilation for near-term algorithms with openpulse, in *53rd Annual IEEE/ACM International Symposium on Microarchitecture, MICRO 2020, Athens, Greece, October 17-21, 2020* (IEEE, 2020) pp. 186–200.

[37] K. N. Smith, G. S. Ravi, T. Alexander, N. T. Bronn, A. Carvalho, A. Cervera-Lierta, F. T. Chong, J. M. Chow, M. Cubeddu, A. Hashim, L. Jiang, O. Lanes, M. J. Otten, D. I. Schuster, P. Gokhale, N. Earnest, and A. Galda, Summary: Chicago quantum exchange (cqe) pulse-level quantum control workshop (2022), [arXiv:2202.13600](https://arxiv.org/abs/2202.13600).

[38] P. Gokhale, Y. Ding, T. Propson, C. Winkler, N. Leung, Y. Shi, D. I. Schuster, H. Hoffmann, and F. T. Chong, Partial compilation of variational algorithms for noisy intermediate-scale quantum machines, in *Proceedings of the 52nd Annual IEEE/ACM International Symposium on Microarchitecture*, MICRO '52 (Association for Computing Machinery, New York, NY, USA, 2019) p. 266–278.

[39] Y. Shi, N. Leung, P. Gokhale, Z. Rossi, D. I. Schuster, H. Hoffmann, and F. T. Chong, Optimized compilation of aggregated instructions for realistic quantum computers, in *Proceedings of the Twenty-Fourth International Conference on Architectural Support for Programming Languages and Operating Systems*, ASPLOS '19 (Association for Computing Machinery, New York, NY, USA, 2019) p. 1031–1044.

[40] P. Gokhale, T. Tomesh, M. Suchara, and F. T. Chong, Faster and more reliable quantum swaps via native gates (2021), [arXiv:2109.13199](https://arxiv.org/abs/2109.13199).

[41] P. D. Nation and M. Treinish, Suppressing quantum circuit errors due to system variability, *PRX Quantum* **4**, 010327 (2023).

[42] S. Brandhofer, D. Braun, V. Dehn, G. Hellstern, M. Hüls, Y. Ji, I. Polian, A. S. Bhatia, and T. Wellens, Benchmarking the performance of portfolio optimization with qaoa, *Quantum Information Processing* **22**, 1 (2023).

[43] Y. Ji, K. F. Koenig, and I. Polian, Optimizing quantum algorithms on bipotent architectures, *Phys. Rev. A* **108**, 022610 (2023).

[44] A. M. Childs, A. Ostrander, and Y. Su, Faster quantum simulation by randomization, *Quantum* **3**, 182 (2019).

[45] P. K. Faehrmann, M. Steudtner, R. Kueng, M. Kieferova, and J. Eisert, Randomizing multi-product formulas for hamiltonian simulation, *Quantum* **6**, 806 (2022).

[46] E. Hellinger, Neue begründung der theorie quadratischer formen von unendlichvielen veränderlichen., *Journal für die reine und angewandte Mathematik* **1909**, 210 (1909).

[47] B. Mohar and S. Poljak, Eigenvalues and the max-cut problem, *Czechoslovak Mathematical Journal* **40**, 343 (1990).

[48] Y. Ji, K. F. Koenig, and I. Polian, Improving the performance of digitized counterdiabatic quantum optimization via algorithm-oriented qubit mapping, *arXiv preprint arXiv:2311.14624* (2023).

[49] A. Peruzzo, J. McClean, P. Shadbolt, M.-H. Yung, X.-Q. Zhou, P. J. Love, A. Aspuru-Guzik, and J. L. O'brien, A variational eigenvalue solver on a photonic quantum processor, *Nature communications* **5**, 1 (2014).

[50] J. Tilly, H. Chen, S. Cao, D. Picozzi, K. Setia, Y. Li, E. Grant, L. Wossnig, I. Runger, G. H. Booth, *et al.*, The variational quantum eigensolver: a review of methods and best practices, *Physics Reports* **986**, 1 (2022).

[51] D. A. Fedorov, B. Peng, N. Govind, and Y. Alexeev, Vqe method: A short survey and recent developments, *Materials Theory* **6**, 1 (2022).

[52] Y. Cao, J. Romero, J. P. Olson, M. Degroote, P. D. Johnson, M. Kieferová, I. D. Kivlichan, T. Menke, B. Peropadre, N. P. Sawaya, *et al.*, Quantum chemistry in the age of quantum computing, *Chemical reviews* **119**, 10856 (2019).

[53] B. Bauer, S. Bravyi, M. Motta, and G. K.-L. Chan, Quantum algorithms for quantum chemistry and quantum materials science, *Chemical Reviews* **120**, 12685 (2020).

[54] D. Amaro, C. Modica, M. Rosenkranz, M. Fiorentini, M. Benedetti, and M. Lubasch, Filtering variational quantum algorithms for combinatorial optimization, *Quantum Science and Technology* **7**, 015021 (2022).

[55] J. Romero, R. Babbush, J. R. McClean, C. Hempel, P. J. Love, and A. Aspuru-Guzik, Strategies for quantum computing molecular energies using the unitary coupled cluster ansatz, *Quantum Science and Technology* **4**, 014008 (2018).

- [56] D. Wecker, M. B. Hastings, and M. Troyer, Progress towards practical quantum variational algorithms, *Physical Review A* **92**, 042303 (2015).
- [57] G. Nannicini, Performance of hybrid quantum-classical variational heuristics for combinatorial optimization, *Phys. Rev. E* **99**, 013304 (2019).
- [58] F. Arute, K. Arya, R. Babbush, D. Bacon, J. C. Bardin, R. Barends, R. Biswas, S. Boixo, F. G. Brandao, D. A. Buell, *et al.*, Quantum supremacy using a programmable superconducting processor, *Nature* **574**, 505 (2019).
- [59] J. S. Otterbach, R. Manenti, N. Alidoust, A. Bestwick, M. Block, B. Bloom, S. Caldwell, N. Didier, E. S. Fried, S. Hong, *et al.*, Unsupervised machine learning on a hybrid quantum computer, arXiv preprint arXiv:1712.05771 (2017).
- [60] K. Georgopoulos, C. Emery, and P. Zuliani, Modeling and simulating the noisy behavior of near-term quantum computers, *Physical Review A* **104**, 062432 (2021).
- [61] J. Zeng, Z. Wu, C. Cao, C. Zhang, S.-Y. Hou, P. Xu, and B. Zeng, Simulating noisy variational quantum eigensolver with local noise models, *Quantum Engineering* **3**, e77 (2021).